

other H3 variants, the possibility of a CENP-A nucleosome composed of one of each core histone (hemisome) is an attractive proposition. However, our findings support the octasome model for the CENP-A nucleosome. It is still possible that both types of CENP-A nucleosomes, octasome and hemisome, coexist in the functional centromeric chromatin *in vivo*. We also cannot exclude the possibility that CENP-A hemisomes can be reconstituted under different conditions and/or with factor(s) required for their assembly. Nevertheless, the present structure suggests that the fundamental principles involved in nucleosome formation are likely to be similar among the H3 variants, including CENP-A. The flexibility exclusively observed in the DNA regions located at the entrance and the exit of the CENP-A nucleosome and the loop 1 region protruding from the CENP-A nucleosome may have an essential role in the centromeric chromatin architecture.

## METHODS SUMMARY

Human CENP-A, H2A, H2B, H3.1 and H4 were overexpressed in *Escherichia coli* cells, and were purified by a method described previously<sup>21,23–25</sup>. Details are provided in Methods. The 147-base-pair DNA used in the CENP-A nucleosome reconstitution was prepared by self-ligation with the 71-base-pair fragment of a human  $\alpha$ -satellite sequence<sup>16,21</sup>, containing an extra 5-base overhang, 5'-GTAAC-3', for the cohesive end. The resultant 147-base-pair DNA contained the CENP-B box near both edges, and an A:A mismatch was located at the centre of the DNA (Supplementary Fig. 2). The preparation, crystallization and structural determination of the CENP-A nucleosome are described in Methods. Analyses of the fluorescent protein-tagged CENP-A or CENP-A mutant incorporation at centromeres were performed using hTERT-RPE1 cells. Details are described in Methods.

**Full Methods** and any associated references are available in the online version of the paper at [www.nature.com/nature](http://www.nature.com/nature).

Received 29 August 2010; accepted 1 June 2011.

Published online 10 July 2011.

- Cheeseman, I. M. & Desai, A. Molecular architecture of the kinetochore-microtubule interface. *Nature Rev. Mol. Cell Biol.* **9**, 33–46 (2008).
- Santaguida, S. & Musacchio, A. The life and miracles of kinetocores. *EMBO J.* **28**, 2511–2531 (2009).
- Palmer, D. K., O'Day, K., Wener, M. H., Andrews, B. S. & Margolis, R. L. A 17-kD centromere protein (CENP-A) copurifies with nucleosome core particles and with histones. *J. Cell Biol.* **104**, 805–815 (1987).
- Stoler, S., Keith, K. C., Curnick, K. E. & Fitzgerald-Hayes, M. A mutation in CSE4, an essential gene encoding a novel chromatin-associated protein in yeast, causes chromosome nondisjunction and cell cycle arrest at mitosis. *Genes Dev.* **9**, 573–586 (1995).
- Meluh, P. B., Yang, P., Glowczewski, L., Koshland, D. & Smith, M. M. Cse4p is a component of the core centromere of *Saccharomyces cerevisiae*. *Cell* **94**, 607–613 (1998).
- Buchwitz, B. J., Ahmad, K., Moore, L. L., Roth, M. B. & Henikoff, S. A histone-H3-like protein in *C. elegans*. *Nature* **401**, 547–548 (1999).
- Henikoff, S., Ahmad, K., Platero, J. S. & van Steensel, B. Heterochromatic deposition of centromeric histone H3-like proteins. *Proc. Natl Acad. Sci. USA* **97**, 716–721 (2000).
- Howman, E. V. *et al.* Early disruption of centromeric chromatin organization in centromere protein A (*Cenpa*) null mice. *Proc. Natl Acad. Sci. USA* **97**, 1148–1153 (2000).
- Takahashi, K., Chen, E. S. & Yanagida, M. Requirement of Mis6 centromere connector for localizing a CENP-A-like protein in fission yeast. *Science* **288**, 2215–2219 (2000).
- Blower, M. D. & Karpen, G. H. The role of *Drosophila* CID in kinetochore formation, cell-cycle progression and heterochromatin interactions. *Nature Cell Biol.* **3**, 730–739 (2001).
- Oegema, K., Desai, A., Rybina, S., Kirkham, M. & Hyman, A. A. Functional analysis of kinetochore assembly in *Caenorhabditis elegans*. *J. Cell Biol.* **153**, 1209–1226 (2001).
- Régnier, V. *et al.* CENP-A is required for accurate chromosome segregation and sustained kinetochore association of BubR1. *Mol. Cell Biol.* **25**, 3967–3981 (2005).
- Luger, K., Mäder, A. W., Richmond, R. K., Sargent, D. F. & Richmond, T. J. Crystal structure of the nucleosome core particle at 2.8 Å resolution. *Nature* **389**, 251–260 (1997).
- Talbert, P. B. & Henikoff, S. Histone variants—ancient wrap artists of the epigenome. *Nature Rev. Mol. Cell Biol.* **11**, 264–275 (2010).
- Yoda, K. *et al.* Human centromere protein A (CENP-A) can replace histone H3 in nucleosome reconstitution *in vitro*. *Proc. Natl Acad. Sci. USA* **97**, 7266–7271 (2000).
- Tanaka, Y. *et al.* Human centromere protein B induces translational positioning of nucleosomes on alpha-satellite sequences. *J. Biol. Chem.* **280**, 41609–41618 (2005).
- Camahort, R. *et al.* Cse4 is part of an octameric nucleosome in budding yeast. *Mol. Cell* **35**, 794–805 (2009).
- Dalal, Y., Wang, H., Lindsay, S. & Henikoff, S. Tetrameric structure of centromeric nucleosomes in interphase *Drosophila* cells. *PLoS Biol.* **5**, e218 (2007).
- Dalal, Y., Furuyama, T., Vermaak, D. & Henikoff, S. Structure, dynamics, and evolution of centromeric nucleosomes. *Proc. Natl Acad. Sci. USA* **104**, 15974–15981 (2007).
- Furuyama, T. & Henikoff, S. Centromeric nucleosomes induce positive DNA supercoils. *Cell* **138**, 104–113 (2009).
- Tanaka, Y. *et al.* Expression and purification of recombinant human histones. *Methods* **33**, 3–11 (2004).
- Tsunaka, Y., Kajimura, N., Tate, S. & Morikawa, K. Alteration of the nucleosomal DNA path in the crystal structure of a human nucleosome core particle. *Nucleic Acids Res.* **33**, 3424–3434 (2005).
- Tachiwana, H. *et al.* Structural basis of instability of the nucleosome containing a testis-specific histone variant, human H3T. *Proc. Natl Acad. Sci. USA* **107**, 10454–10459 (2010).
- Tachiwana, H., Osakabe, A., Kimura, H. & Kurumizaka, H. Nucleosome formation with the testis-specific histone H3 variant, H3t, by human nucleosome assembly proteins *in vitro*. *Nucleic Acids Res.* **36**, 2208–2218 (2008).
- Osakabe, A. *et al.* Nucleosome formation activity of human somatic nuclear autoantigenic sperm protein (sNASP). *J. Biol. Chem.* **285**, 11913–11921 (2010).
- Sekulic, N., Bassett, E. A., Rogers, D. J. & Black, B. E. The structure of (CENP-A-H4)<sub>2</sub> reveals physical features that mark centromeres. *Nature* **467**, 347–351 (2010).
- Conde e Silva, N. *et al.* CENP-A-containing nucleosomes: easier disassembly versus exclusive centromeric localization. *J. Mol. Biol.* **370**, 555–573 (2007).
- Kingston, I. J., Yung, J. S. & Singleton, M. R. Biophysical characterisation of the centromere-specific nucleosome from budding yeast. *J. Biol. Chem.* **286**, 4021–4026 (2011).
- Schalch, T., Duda, S., Sargent, D. F. & Richmond, T. J. X-ray structure of a tetranucleosome and its implications for the chromatin fibre. *Nature* **436**, 138–141 (2005).
- Masumoto, H., Masukata, H., Muro, Y., Nozaki, N. & Okazaki, T. A human centromere antigen (CENP-B) interacts with a short specific sequence in alphoid DNA, a human centromeric satellite. *J. Cell Biol.* **109**, 1963–1973 (1989).

**Supplementary Information** is linked to the online version of the paper at [www.nature.com/nature](http://www.nature.com/nature).

**Acknowledgements** We thank the beamline scientists, N. Shimizu, Y. Kawano, M. Makino and T. Hikima, for their assistance with data collection at the BL41XU and BL45XU beamlines of SPring-8. We also thank R. Matsumoto for technical assistance, K. Yoda for anti-CENP-C, and T. Fukagawa and Y. Hiraoka for discussions. This work was supported in part by Grants-in-Aid from the Japanese Society for the Promotion of Science (JSPS), and the Ministry of Education, Culture, Sports, Science and Technology (MEXT), Japan. H.Ku. was also supported by the Waseda Research Institute for Science and Engineering.

**Author Contributions** H.T., T.S., A.O. and Y.M. purified the histones and CENP-A, crystallized the CENP-A nucleosome, and performed biochemical analyses. H.T., W.K., K.S. and T.S. collected X-ray diffraction data, and H.T., W.K., and S.-Y.P. performed the structural analysis of the CENP-A nucleosome. H.T., A.O., Y.H.-T. and H.Ki. performed the cell biological experiments. T.O., H.T., W.K. and M.S. performed SAXS analysis. H.Ku. conceived, designed and supervised all of the work, and H.Ku., W.K. and H.T. wrote the paper. All of the authors discussed the results and commented on the manuscript.

**Author Information** The atomic coordinates of the CENP-A nucleosome have been deposited in the Protein Data Bank, under the accession code 3AN2. Reprints and permissions information is available at [www.nature.com/reprints](http://www.nature.com/reprints). The authors declare no competing financial interests. Readers are welcome to comment on the online version of this article at [www.nature.com/nature](http://www.nature.com/nature). Correspondence and requests for materials should be addressed to H.Ku. ([kurumizaka@waseda.jp](mailto:kurumizaka@waseda.jp)).

## METHODS

**Overexpression of human histones.** Human histones H2A and H2B were produced in *Escherichia coli* BL21(DE3) cells, and histone H4 was produced in *E. coli* JM109(DE3) cells. Human CENP-A was produced in *E. coli* DH5 $\alpha$  cells. All histones and CENP-A were produced in *E. coli* cells in the absence of T7 RNA polymerase by omitting the addition of isopropyl- $\beta$ -D-thiogalactopyranoside, which induces the T7 RNA polymerase production in BL21(DE3) and JM109(DE3) cells. All histones and CENP-A were produced as N-terminal His<sub>6</sub>-tagged proteins, as described previously<sup>21</sup>. The His<sub>6</sub> tags of all histones were removed by thrombin protease digestion, leaving a Gly-Ser-His sequence at the N-terminal end of each histone.

For the purpose of structural determination, selenomethionine (Se-Met)-substituted H2B was produced in *E. coli* B834(DE3) cells, using the pET15b vector system (Novagen). The B834(DE3) cells were grown in 100 ml of LB medium for 4 h at 37 °C. The cells were collected and transferred into 300 ml of M9 medium (+50  $\mu$ g ml<sup>-1</sup> Se-Met). After 12 h growth at 37 °C, the 300-ml culture was added to 2 l of M9 medium (+50  $\mu$ g ml<sup>-1</sup> Se-Met), and the culture was continued at 37 °C. When the cell density reached 0.5 ( $D_{600}$ ), isopropyl- $\beta$ -D-thiogalactopyranoside (final concentration 1 mM) was added, to induce the expression of H2B. The cells were grown further at 37 °C for 12 h.

**Purification of human histones.** The cells producing recombinant histones were collected, and were resuspended in 50 ml of buffer A (50 mM Tris-HCl (pH 8.0), 500 mM NaCl, 1 mM PMSF and 5% glycerol). The cells were disrupted by two rounds of sonication for 200 s each. The cell lysates were centrifuged at 27,216g for 20 min at 4 °C. The supernatants were discarded, and the pellet containing the His<sub>6</sub>-tagged histones was resuspended in 50 ml of buffer A, containing 7 M guanidine hydrochloride. The samples were rotated for 12 h at 4 °C, and the supernatants were recovered by centrifugation at 27,216g for 20 min at 4 °C. The supernatants containing the His<sub>6</sub>-tagged histones were combined with 4 ml (50% slurry) of nickel-nitrilotriacetic acid (Ni-NTA) agarose resin (Qiagen), and the samples were rotated for 1 h at 4 °C. The agarose beads were then washed with 100 ml of buffer B (50 mM Tris-HCl (pH 8.0), 500 mM NaCl, 6 M urea, 5 mM imidazole, and 5% glycerol). The His<sub>6</sub>-tagged histones were eluted by a 100-ml linear gradient of 5 to 500 mM imidazole in buffer B, and the samples were dialysed against buffer C (5 mM Tris-HCl (pH 7.5) and 2 mM 2-mercaptoethanol). The N-terminal His<sub>6</sub> tags were removed from the histones by thrombin protease treatment (1 unit mg<sup>-1</sup> of histones; GE Healthcare) at room temperature for 3 h. The removal of the His<sub>6</sub> tags was confirmed by SDS-16% polyacrylamide gel electrophoresis (PAGE); the recombinant histones without the His<sub>6</sub> tag migrated faster than the His<sub>6</sub>-tagged histones. After the His<sub>6</sub> tag was uncoupled, each histone was subjected to Mono S column chromatography (GE Healthcare). The column was washed with buffer D (20 mM sodium acetate (pH 5.2), 200 mM NaCl, 5 mM 2-mercaptoethanol, 1 mM EDTA, and 6 M urea), and each histone was eluted by a linear gradient of 200 to 800 mM NaCl in buffer D. The purified histones were dialysed against water, and were freeze-dried.

**Preparation of DNAs.** The 147-base-pair DNA, which was used for reconstituting the CENP-A nucleosome, is a derivative of the human  $\alpha$ -satellite DNA (sat4)<sup>21</sup>. The EcoRI site (GAATTC) of the sat4 sequence was replaced by a BstPI site (GGTAAACC). The 71-mer DNA fragment containing the 5' half of the sat4 sequence, with the CENP-B box at the edge, was ligated in tandem in the plasmid (p5'Sat4-24). The 71-mer DNA fragment containing an extra 5-base overhang, 5'-GTAAC-3', was prepared for self-ligation according to the method described previously<sup>31</sup>. The 71-mer DNA fragment containing the 5-base overhang was self-ligated, and the palindromic 147-base-pair  $\alpha$ -satellite DNA derivative was prepared. The 147-base-pair DNA sequence is: 5'-ATCCTTCGTTGGAAACGGGATTTCTTTCATTTTCATGCTAGACAGAAGAATTCTCAGTAACTTCTTTG TGCTGGTAAACGACACAAAGAAGTTACTGAGAATTCTTCTGTCTAGCAT GAAATGAAGAAATCCCGTTTCCAACGAAGGAT-3'.

In this palindromic 147-base-pair  $\alpha$ -satellite DNA derivative, an A:A mismatch was introduced at the centre of the 147-base-pair DNA fragment (underlined).

**Preparation of the CENP-A nucleosome.** The purified H2A-H2B (Se-Met)-CENP-A-H4 (0.9 mg) and the 147-base-pair DNA (1 mg) were mixed in a solution containing 2 M KCl, and the sample was dialysed against dialysis buffer (10 mM Tris-HCl (pH 7.5), 1 mM EDTA, 1 mM dithiothreitol and 2 M KCl). After dialysis at 4 °C for 3 h, the KCl concentration of the dialysis buffer was gradually decreased to 250 mM with a peristaltic pump (0.8 ml min<sup>-1</sup> flow rate). The sample was then dialysed against 10 mM Tris-HCl buffer (pH 7.5), containing 1 mM EDTA, 1 mM dithiothreitol and 250 mM KCl, at 4 °C for 3 h. After this dialysis step, the sample was incubated at 55 °C for 2 h. The CENP-A nucleosome was purified from the free DNA and histones by non-denaturing polyacrylamide gel electrophoresis, using a Prep Cell apparatus (Bio-Rad). The purified CENP-A nucleosome was concentrated, and was dialysed against 20 mM potassium cacodylate buffer (pH 6.0) containing 1 mM EDTA.

**Crystallization and structure determination.** Crystals of the purified CENP-A nucleosome were obtained by the hanging drop method, after mixing equal volumes of the CENP-A nucleosome solution and 20 mM potassium cacodylate buffer (pH 6.0), containing 60–96 mM KCl and 135–144 mM MnCl<sub>2</sub>. The CENP-A nucleosome sample was equilibrated against a reservoir solution of 20 mM potassium cacodylate (pH 6.0), 38–56 mM KCl, and 70–75 mM MnCl<sub>2</sub>. Crystals of the CENP-A nucleosome were soaked in a cryoprotectant solution, containing 20 mM potassium cacodylate (pH 6.0), 47 mM KCl, 72 mM MnCl<sub>2</sub>, 30% polyethylene glycol 400, and 5% trehalose. The crystals were flash-cooled in a stream of N<sub>2</sub> gas (100 K). The CENP-A nucleosome crystals belonged to the monoclinic space group *P*2<sub>1</sub>, with unit cell constants of  $a = 65.8 \text{ \AA}$ ,  $b = 83.3 \text{ \AA}$ ,  $c = 176.8 \text{ \AA}$  and  $\beta = 100.7^\circ$ , and contained one nucleosome in the asymmetric unit. High-resolution diffraction data were obtained using the synchrotron radiation source at the beamline BL41XU station of SPring-8, Harima, Japan.

Diffraction data of the CENP-A nucleosome were integrated and scaled with the HKL2000 program<sup>32</sup>. The data were processed with the CCP4 program suite<sup>33</sup>. The structure was solved by the molecular replacement method, using the MOLREP program<sup>34</sup> and the human nucleosome structure (PDB accession number 3AFA) as a search model<sup>33</sup>. Most of the amino acid side chains were clearly visible in the map initially calculated at 3.6  $\text{\AA}$  resolution. Rigid body refinement of the obtained solution was performed using the CNS program<sup>35</sup>. Further structural refinement consisted of iterative rounds of energy minimization and B factor refinement using the CNS program<sup>35</sup>, and model building using the COOT program<sup>36</sup>. The Ramachandran plot of the final structure showed 98.7% of the residues in the most favourable and additional allowed regions, and no residues in the disallowed region. Summaries of the data collection and refinement statistics are provided in Supplementary Table 1. All structure figures were created using the PyMOL program (<http://pymol.org>). The atomic coordinates of the CENP-A nucleosome have been deposited in the Protein Data Bank, with the ID code 3AN2.

**Supercoupling assay.** Salt-dialysis supercoupling assay. Relaxed plasmid DNA (500 ng) was mixed with 0, 125, 250, 500 and 1,000 ng of histone octamer in 5  $\mu$ l of 20 mM Tris-HCl (pH 7.5) buffer, containing 1 mM EDTA, 0.2 mg ml<sup>-1</sup> BSA, and 2 M NaCl. The samples were then incubated at 37 °C for 30 min. The NaCl concentration of the sample was reduced to 1 M, 0.8 M, 0.67 M, and 0.2 M by adding dilution buffer, containing 20 mM Tris-HCl (pH 7.5), 1 mM EDTA, 0.2 mg ml<sup>-1</sup> BSA, 5 mM MgCl<sub>2</sub>, and 0.06 U  $\mu$ l<sup>-1</sup> calf (Invitrogen) or wheat germ (Promega) topoisomerase I. The samples were incubated at 37 °C for 30 min in each dilution step.

Chaperone-mediated supercoupling assay. NAP1 or sNASP (0.25, 0.5, and 1.0  $\mu$ M) was pre-incubated with H2A-H2B (150 ng) and CENP-A-H4 (150 ng) at 37 °C for 15 min. Supercoupled plasmid DNA (100 ng), which was relaxed with a topoisomerase I solution (10 mM Tris-HCl (pH 8.0), 2 mM MgCl<sub>2</sub>, 5 mM dithiothreitol, and 2 U  $\mu$ l<sup>-1</sup> wheat germ topoisomerase I (Promega)), was added to the reaction mixture. The samples were then incubated at 37 °C for 60 min in 10 mM Tris-HCl (pH 8.0) buffer, containing 140 mM NaCl, 2 mM MgCl<sub>2</sub>, and 5 mM dithiothreitol, followed by an incubation at 42 °C for 60 min.

In both the salt-dialysis and chaperone-mediated assays, after the reaction, the samples were treated with 50  $\mu$ l of a proteinase K solution (20 mM Tris-HCl (pH 8.0), 20 mM EDTA, 0.5% SDS, and 0.5 mg ml<sup>-1</sup> proteinase K (Roche)) at 37 °C for 30 min. The DNA was extracted with phenol/chloroform. The DNA was then precipitated by ethanol, and was analysed by one-dimensional gel electrophoresis on a 1% agarose gel in 1  $\times$  TAE buffer (for the salt-dialysis assay, 1.3 V cm<sup>-1</sup> for 15.5 h) or 1  $\times$  TBE buffer (for the chaperone-mediated assay, 1.3 V cm<sup>-1</sup> for 15.5 h). For the two-dimensional gel electrophoresis, the DNA was electrophoresed on a 0.7% agarose gel in 1  $\times$  TBE buffer (for the salt-dialysis assay, 2 V cm<sup>-1</sup> for 7 h) or a 1% agarose gel in 1  $\times$  TBE buffer (for the chaperone-mediated assay, 1.3 V cm<sup>-1</sup> for 15 h) for the first dimension. The gel was then soaked in 1  $\times$  TBE buffer containing 4 mg l<sup>-1</sup> of chloroquine for 3 h. The samples were subsequently electrophoresed in 1  $\times$  TBE buffer containing 4 mg l<sup>-1</sup> of chloroquine (1.3 V cm<sup>-1</sup> for 12 h (for the salt-dialysis assay) or 1.3 V cm<sup>-1</sup> for 15 h (for the chaperone-mediated assay)) for the second dimension. The DNA was visualized by SYBR Gold (Invitrogen) staining.

**Nucleosome reconstitution by the salt-dialysis method for biochemical analyses.** The purified H2A-H2B-CENP-A-H4 or H2A-H2B-H3-H4 octamer was mixed with a DNA fragment (300  $\mu$ g, 121-base-pair DNA or 147-base-pair DNA) in a solution containing 2 M KCl (376  $\mu$ l). The amounts of histone octamers were 420  $\mu$ g for the 121-base-pair DNA and 384  $\mu$ g for the 147-base-pair DNA. Nucleosomes were reconstituted and prepared by the same method as described in the 'Preparation of the CENP-A nucleosome' section.

**Competitive nucleosome assembly assay.** The purified H2A-H2B-CENP-A-H4 octamer (14, 28, 42 or 56  $\mu$ g) was incubated in the presence of both the 147-base-pair DNA (24  $\mu$ g) and 121-base-pair DNA (20  $\mu$ g), in a solution containing 2 M KCl, and the sample was dialysed against dialysis buffer (10 mM Tris-HCl

(pH 7.5), 1 mM EDTA, 1 mM dithiothreitol, and 2 M KCl). After dialysis at 4 °C for 3 h, the KCl concentration of the dialysis buffer was gradually decreased to 250 mM with a peristaltic pump (0.8 ml min<sup>-1</sup> flow rate). The sample was then dialysed against 10 mM Tris-HCl buffer (pH 7.5), containing 1 mM EDTA, 1 mM dithiothreitol, and 250 mM KCl, at 4 °C for 3 h. The CENP-A nucleosomes were then analysed by 6% PAGE in 0.2× TBE buffer (18 mM Tris base, 18 mM boric acid, and 0.4 mM EDTA) at 16 V cm<sup>-1</sup> for 1 h, followed by ethidium bromide staining.

**Nucleosome disruption assay.** The CENP-A nucleosomes were reconstituted with a 121-base-pair or 147-base-pair palindromic  $\alpha$ -satellite derivative, by the salt dialysis method. The 121-base-pair DNA lacks the 13-base-pair regions from both edges of the 147-base-pair DNA used in the crystallography of the CENP-A nucleosome. The rest of the 121-base-pair DNA sequence is identical to the 147-base-pair palindromic  $\alpha$ -satellite derivative. The CENP-A nucleosomes (150 ng) were incubated at 37 °C, 57 °C, 67 °C, 70 °C, or 73 °C for 15 min in the presence of supercoiled plasmid DNA (100 ng). After the incubation, the CENP-A nucleosomes that were not disrupted were separated by non-denaturing 6% PAGE, and were visualized by ethidium bromide staining. The relative band intensities for the CENP-A nucleosomes were quantified and plotted against the temperature.

**Exonuclease assay.** The reconstituted CENP-A or H3 nucleosomes were treated with 3 units of *Escherichia coli* exonuclease III (Takara), in 10  $\mu$ l of 50 mM Tris-HCl (pH 8.0), 5 mM MgCl<sub>2</sub>, and 1 mM DTT. After an incubation for 0, 2, 4, or 8 min at 37 °C, the reaction was stopped by the addition of 55  $\mu$ l of proteinase K solution (20 mM Tris-HCl (pH 8.0), 20 mM EDTA, 0.5% SDS, and 0.5 mg ml<sup>-1</sup> proteinase K (Roche)). After a 15 min incubation at room temperature, the DNA was extracted with phenol/chloroform, precipitated with ethanol, dissolved in Hi-Di Formamide (Applied Biosystems), and then analysed by 10% denaturing PAGE with a gel containing 7 M urea in 0.5× TBE buffer (21 V cm<sup>-1</sup> for 1.5 h).

**Small-angle X-ray scattering (SAXS).** SAXS measurements of the reconstituted CENP-A and H3 nucleosomes, in 20 mM Tris-HCl buffer (pH 7.5) containing 1 mM EDTA and 1 mM DTT, were performed at the RIKEN structural biology beam-line I (BL45XU) of SPring-8 (Hyogo, Japan)<sup>37</sup>. Scattering intensities of the nucleosome solutions were measured with an R-AXIS IV<sup>++</sup> imaging plate detector at 20 °C with a sample-to-detector distance of 3,529 mm, which was calibrated by the powder diffraction from silver dicosanoate. Circular averaging of the scattering intensities was then performed to obtain the one-dimensional scattering data  $I(q)$  as a function of  $q$  ( $q = 4\pi\sin\theta/\lambda$ ), where  $2\theta$  is the scattering angle and the X-ray wavelength  $\lambda = 0.9$  Å. Three successive measurements were made for each solution, with an exposure time of 60 s. The resultant three data sets were combined after inspections for X-ray radiation damage to the solution and the existence of instrumental artefacts. SAXS measurements of the buffer solution for background subtraction were performed after each measurement of the nucleosome solutions, using the same conditions and procedure as those of the nucleosome solutions. To correct the inter-particle interference effect,  $I(q)$  data were collected at four protein concentrations (0.5, 0.7, 1.0 and 1.3 mg ml<sup>-1</sup>), and extrapolated to zero concentration. The data were processed and analysed using the software applications embedded in the ATSAS package ([http://www.](http://www.embl-hamburg.de/biosaxs/software.html)

<http://www.embl-hamburg.de/biosaxs/software.html>). The radius of gyration,  $R_g$ , was estimated by fitting the  $I(q)$  data using the Guinier approximation  $I(q) = I(0) \exp(-q^2 R_g^2/3)$ , where  $I(0)$  is the forward scattering at the zero scattering angle, in a smaller angle region of  $qR_g < 1.3$ . Error of  $R_g$  was estimated from the least-squares fitting. The distance distribution function  $P(r)$  and its error were calculated by the program GNOM<sup>38</sup>. The maximum dimension  $D_{max}$  was estimated from the  $P(r)$  function as the distance  $r$ , where  $P(r) = 0$  (ref. 39), and its error was estimated from the errors of the  $P(r)$  values around  $P(r) = 0$ .

**Centromere localization of CENP-A and CENP-A mutants.** hTERT-RPE1 cells were transfected with combinations of wild-type CENP-A and CENP-A(del), in which two amino acid residues (the Arg 80 and Gly 81 residues of the CENP-A loop 1) were deleted, and tagged with either GFP or RFP, using GeneJuice (Merck) according to the manufacturer's instructions. hTERT-RPE1 cells were also transfected with combinations of wild-type CENP-A tagged with RFP and CENP-A(del82-83) (where the Val 82 and Asp 83 residues of the CENP-A loop 1 were deleted), or CENP-A(A80A81) (where the Arg 80 and Gly 81 residues were replaced by Ala 80 and Ala 81), or CENP-A(A82A83) (where the Val 82 and Asp 83 residues were replaced by Ala 82 and Ala 83), tagged with GFP. The cells were fixed with 4% paraformaldehyde 1–3 days after transfection, permeabilized, and stained with guinea pig anti-CENP-C<sup>40</sup> and donkey Cy5-conjugated anti-guinea pig Ig (Jackson ImmunoResearch). DNA was counterstained with 12.5 ng ml<sup>-1</sup> DAPI. The fluorescence images were collected using an inverted microscope (Ti-E; Nikon) with a  $\times 100$  PlanApo VC numerical aperture (NA) = 1.4 oil-immersion objective lens, or a  $\times 40$  PlanApo NA = 0.95 dry lens, equipped with an EM-CCD camera (iXon+; Andor). The numbers of transfected cells exhibiting the GFP- or RFP-tagged protein, or both, at the centromeres were counted, and the average percentages from three independent transfections were plotted with the standard deviations.

31. Dyer, P. N. *et al.* Reconstitution of nucleosome core particles from recombinant histones and DNA. *Methods Enzymol.* **375**, 23–44 (2003).
32. Otwinowski, Z. & Minor, W. Processing of X-ray diffraction data collected in oscillation mode. *Methods Enzymol.* **276**, 307–326 (1997).
33. Collaborative Computational Project, Number 4. The CCP4 suite: programs for protein crystallography. *Acta Crystallogr. D* **50**, 760–763 (1994).
34. Vagin, A. & Teplyakov, A. *MOLREP*: an automated program for molecular replacement. *J. Appl. Cryst.* **30**, 1022–1025 (1997).
35. Brünger, A. T. *et al.* *Crystallography & NMR system*: A new software suite for macromolecular structure determination. *Acta Crystallogr. D* **54**, 905–921 (1998).
36. Emsley, P., Lohkamp, B., Scott, W. G. & Cowtan, K. Features and development of *Coot*. *Acta Crystallogr. D* **66**, 486–501 (2010).
37. Fujisawa, T. *et al.* Small-angle X-ray scattering station at the SPring-8 RIKEN beamline. *J. Appl. Cryst.* **33**, 797–800 (2000).
38. Svergun, D. I. Determination of the regularization parameter in indirect-transform methods using perceptual criteria. *J. Appl. Cryst.* **25**, 495–503 (1992).
39. Glatter, O. & Kratky, O. *Small-angle X-ray Scattering* (Academic Press, 1982).
40. Ando, S. *et al.* CENP-A, -B, and -C chromatin complex that contains the l-type  $\alpha$ -satellite array constitutes the prekinetochore in HeLa cells. *Mol. Cell. Biol.* **22**, 2229–2241 (2002).

# Oxygen Binding and Redox Properties of the Heme in Soluble Guanylate Cyclase

## IMPLICATIONS FOR THE MECHANISM OF LIGAND DISCRIMINATION<sup>\*[E]</sup>

Received for publication, August 20, 2010, and in revised form, January 26, 2011. Published, JBC Papers in Press, March 8, 2011, DOI 10.1074/jbc.M110.177576

Ryu Makino<sup>+1</sup>, Sam-yon Park<sup>5</sup>, Eiji Obayashi<sup>5</sup>, Tetsutaro Iizuka<sup>¶</sup>, Hiroshi Hori<sup>||</sup>, and Yoshitugu Shiro<sup>¶</sup>

From the <sup>+</sup>Department of Life Science, College of Science, Rikkyo University, Nishi-ikebukuro 3-34-1, Toshima-ku, Tokyo 171-8501, Japan, the <sup>5</sup>Protein Design Laboratory, Yokohama City University, 1-7-29 Suehiro, Tsurumi, Yokohama 230-0045, Japan, <sup>¶</sup>RIKEN Harima Institute/Spring 8, 1-1-1 Kouto, Mikazuki-cho, Sayo-gun, Hyogo 679-5148, Japan, and the <sup>||</sup>Center for Quantum Science and Technology under Extreme Conditions, Osaka University, Toyonaka, Osaka 560-8531, Japan

Soluble guanylate cyclase is an NO-sensing hemoprotein that serves as a NO receptor in NO-mediated signaling pathways. It has been believed that this enzyme displays no measurable affinity for O<sub>2</sub>, thereby enabling the selective NO sensing in aerobic environments. Despite the physiological significance, the reactivity of the enzyme-heme for O<sub>2</sub> has not been examined in detail. In this paper we demonstrated that the high spin heme of the ferrous enzyme converted to a low spin oxyheme (Fe<sup>2+</sup>-O<sub>2</sub>) when frozen at 77 K in the presence of O<sub>2</sub>. The ligation of O<sub>2</sub> was confirmed by EPR analyses using cobalt-substituted enzyme. The oxy form was produced also under solution conditions at -7 °C, with the extremely low affinity for O<sub>2</sub>. The low O<sub>2</sub> affinity was not caused by a distal steric protein effect and by rupture of the Fe<sup>2+</sup>-proximal His bond as revealed by extended x-ray absorption fine structure. The midpoint potential of the enzyme-heme was +187 mV, which is the most positive among high spin protoheme-hemoproteins. This observation implies that the electron density of the ferrous heme iron is relatively low by comparison to those of other hemoproteins, presumably due to the weak Fe<sup>2+</sup>-proximal His bond. Based on our results, we propose that the weak Fe<sup>2+</sup>-proximal His bond is a key determinant for the low O<sub>2</sub> affinity of the heme moiety of soluble guanylate cyclase.

Soluble guanylate cyclase (sGC)<sup>2</sup> is a well characterized NO receptor involved in cell-cell signal transduction pathways associated with neuronal communication and vasodilation (1–7). Mammalian sGC is a heterodimeric (αβ) hemoprotein (8–10) in which the β subunit binds a stoichiometric amount of heme via a weak bond between the heme iron and His-104

(11–14). The binding of NO to the ferrous heme cleaves the weak Fe<sup>2+</sup>-proximal His bond, and the resultant NO complex with 5-coordinate NO heme markedly stimulates the enzymic production of cGMP (9, 14–17). The enzyme-heme also binds carbon monoxide (CO) with moderate stimulation of enzyme activity. It has been thought that the ferrous enzyme-heme in sGC does not exhibit a measurable affinity for O<sub>2</sub> despite having a vacant axial position on the heme (9). This is in contrast to other hemoproteins with a Fe<sup>2+</sup>-proximal His linkage, including globins and heme-containing oxygenases. The lack of affinity for O<sub>2</sub> allows sGC to function as a selective NO-sensor even in the presence of high concentrations of O<sub>2</sub> and prevents oxidation of ferrous heme by O<sub>2</sub>.

We have examined the reaction of the enzyme-heme in sGC with external ligands using a rapid scan-stopped flow method as well as EPR, resonance Raman, and an infrared spectroscopy and established the following. (i) A 5-coordinate NO complex is produced via 6-coordinate NO complex in the reaction with NO (14). (ii) The ferric heme of sGC combines N<sub>3</sub><sup>-</sup> to form a unique 5-coordinate high spin complex with a high cyclase activity (14). (iii) YC-1(3-(5'-hydroxymethyl-3'-furyl)-1-benzylindazole), an allosteric activator, induces the coordination changes in the CO complex from 6-coordinate CO heme to a 5-coordinate CO heme (17). Most of these anomalous heme coordination structures are specific to soluble guanylate cyclase among hemoproteins and seem to be associated with the weak Fe<sup>2+</sup>-proximal His bond.

X-ray Structural analyses of the H-NOX (heme-NO/oxygen binding) or SONO (sensor of nitric oxide) domain, which share considerable sequence homology with the sGC heme domain, have been carried out to identify possible key determinants for modulating the O<sub>2</sub> binding ability of sGC (18, 19). H-NOX/SONO have a proximal His residue that is probably involved in the signaling pathway for O<sub>2</sub> and/or NO. Spectroscopic characterization revealed that the H-NOX/SONO heme sensor domain from *Thermoanaerobacter tengcongensis*, an obligate anaerobe, produced a 6-coordinate NO heme and a stable oxy-heme (Fe<sup>2+</sup>-O<sub>2</sub>), reminiscent of globins (19, 20). By contrast, the H-NOX/SONO protein from *Clostridium botulinum* resembles mammalian and insect sGCs (21) and forms a stable 5-coordinate NO heme but not a stable oxy heme (18). The crystal structure of the oxy form of *T. tengcongensis* H-NOX revealed that a Tyr residue on the distal side of the heme was

<sup>\*</sup> This work was supported by Frontier Project "Life Adaptation Strategies to Environmental Changes" of Rikkyo University and grants-in-aid from the Ministry of Culture, Education, Sports, Science, and Technology of Japan (to R. M.).

<sup>[E]</sup> The on-line version of this article (available at <http://www.jbc.org>) contains supplemental Figs. 1–3.

<sup>1</sup> To whom correspondence should be addressed: Dept. of Life Science, and Frontier Project "Life Adaptation Strategies to Environmental Changes," College of Science, Rikkyo (St. Paul's) University, Nishi-ikebukuro 3-34-1, Toshima-ku, Tokyo 171-8501, Japan. Fax: 81-3-3985-2386; E-mail: rmakino@rikkyo.ne.jp.

<sup>2</sup> The abbreviations used are: sGC, soluble guanylate cyclase;  $K_d$ , dissociation constant;  $k_{on}$ , association rate constant;  $k_{off}$ , dissociation rate constant; EXAFS, extended x-ray absorption fine structure; DMF, dimethylformamide; TEA, triethanolamine.

involved in hydrogen bond formation with the bound O<sub>2</sub> molecule (19). However, H-NOX proteins from facultative aerobes as well as typical NO-regulated sGCs from mammalian sources possess an Ile residue at the position corresponding to the distal Tyr (19). Replacement of the Tyr residue with Ile markedly reduced the O<sub>2</sub> affinity of the heme-domain of the *T. tengcongensis* protein, thereby substantiating the crucial role of the distal Tyr in the discrimination of O<sub>2</sub> binding in the H-NOX proteins (20).

Mammalian sGC contains Ile-145 at the position homologous to the distal Tyr. Boon *et al.* (20) converted the Ile-145 of sGC  $\beta$ -subunit homodimer to Tyr and found that the mutant homodimer produced a stable oxy form, although the affinity for O<sub>2</sub> was extremely low. Hence, it was hypothesized that the absence of a hydrogen-bonding residue in the distal heme pocket is essential for O<sub>2</sub> exclusion by sGC. Martin *et al.* (22) have tested the hypothesis by employing a complete human sGC heterodimer. However, substitution of Ile-145 with Tyr in the  $\beta$ -subunit did not facilitate the binding of O<sub>2</sub> to the enzyme. This unexpected finding may be due to the inappropriate orientation of the Tyr phenolic OH group relative to the ligand. Indeed, a recent publication revealed that an additional mutation, I149E, in the distal pocket enabled the enzyme-heme to react with O<sub>2</sub> (23). The I149E mutation probably induces a repositioning of the phenolic OH group of the introduced Tyr toward the bound O<sub>2</sub>, facilitating the formation of a hydrogen bond. Although the above mutational study demonstrates that a hydrogen bond in the distal pocket is one of the main factors responsible for the stabilization of bound O<sub>2</sub>, the oxy form of the mutant enzyme was still unstable and only detected as a transient species. This finding implies that an additional factor(s) might be involved in the mechanism to control the reactivity of the heme for O<sub>2</sub>. Despite the important implication, detailed experiments to examine the reaction of sGC with O<sub>2</sub> have not been reported. In the present paper we describe the detection and characterization of the oxy form of sGC.

When ferrous sGC was frozen at 77 K, we found that the enzyme-heme converted to a new species with an optical spectrum similar to that of oxyhemoglobin. The new species was also produced under fluid conditions at  $-7^{\circ}\text{C}$ , but the amount was remarkably small, suggesting an extremely low O<sub>2</sub> affinity of the ferrous heme. This species was assigned to be an oxy form by the spectral similarity with oxymyoglobin, by the inhibitory action of isocyanide for the new species formation, and by EPR characterization of the corresponding form of the Co<sup>2+</sup>-porphyrin-substituted enzyme. EXAFS analyses revealed that upon binding O<sub>2</sub>, the ferrous iron in the out-of-plane position moved toward the heme plane without rupture of the Fe<sup>2+</sup>-proximal His bond. These results indicate that the oxy form is in a 6-coordinate state and that the low affinity for O<sub>2</sub> is not caused by cleavage of the Fe<sup>2+</sup>-proximal His bond. Electrochemical analyses revealed that the enzyme-heme had the most positive midpoint potential (+187 mV) among high spin protoheme-containing hemoproteins. This result strongly suggests that the electron density on the ferrous heme in sGC is significantly lowered relative to the ferrous heme of other hemoproteins. The decrease in the electron density, which may be due to the weak Fe<sup>2+</sup>-proximal His bond, weakens the

Fe<sup>2+</sup>-O<sub>2</sub> bond strength as a result of diminished electron donation from iron to O<sub>2</sub>. Our results suggest the weak Fe<sup>2+</sup>-proximal His bond is a critical factor that could account for the lower O<sub>2</sub> affinity of sGC. By contrast, the distal protein effect, comprising steric hindrance in the distal heme pocket, had no significant impact on the ligand binding of sGC.

## EXPERIMENTAL PROCEDURES

**Enzyme Purification**—Fresh bovine lung (5 kg) was minced and homogenized using a Waring blender in 15-liters of 50 mM potassium phosphate buffer, pH 7.4, containing a mixture of protease inhibitors (1 mM phenylmethylsulfonyl fluoride, 1 mM benzamidine, and 1 mM EDTA) and 55 mM  $\beta$ -mercaptoethanol (14, 17, 24). Protease inhibitors and  $\beta$ -mercaptoethanol were included in all the buffers throughout the purification unless stated otherwise. The successive purification steps of the enzyme were the same as those described earlier (24). The purified enzyme preparations were stored in liquid nitrogen until use.

**Spectral Measurements**—The formation of the oxy form was examined under the solution conditions at 3 and  $-7^{\circ}\text{C}$ . The experiments at subzero temperature were carried out in 40 mM TEA buffer, pH 7.5, containing 10% (v/v) ethylene glycol as antifreeze. The temperature of the cuvette holder was maintained at  $-7^{\circ}\text{C}$  or  $3^{\circ}\text{C}$  by thermomodule elements. The fully reduced sGC was added to the anaerobic buffer solution in a septum-sealed anaerobic cuvette that was kept in an anaerobic state by flushing with N<sub>2</sub> gas. The optical absorption spectra under the conditions were recorded on a PerkinElmer Life Sciences Lambda 18 spectrophotometer, and 5–6 scans were averaged to improve the signal to noise ratio. After the spectra of the ferrous enzyme were collected, the solution was kept in two atmospheres of O<sub>2</sub> gas introduced via the septum. Optical spectra were recorded (average of 5–6 scans) after carefully shaking to equilibrate with O<sub>2</sub>.

Optical spectra at 77 K were measured on a Shimadzu MPS-2450 spectrophotometer (Shimadzu, Kyoto, Japan) equipped with a homemade low temperature attachment consisting of a liquid N<sub>2</sub> Dewar and twin cuvettes (light path, 1 mm) for sample and reference solutions, as reported previously (25). To obtain a well balanced spectrum at 77 K, the buffer containing 5% ethylene glycol was employed.

EPR spectra were measured on a Varian E-12 X-band EPR spectrometer (Varian, Palo Alto, CA) with a 100-kHz field modulation. The sample temperature was controlled with an Oxford ESR-900 cryostat as described previously (14, 17).

The iron K-edge EXAFS measurements were performed using synchrotron radiation at station BLC12C of Photon Factory in the National Laboratory of High Energy Physics (Tsukuba, Japan). EXAFS data were collected at 80 K as fluorescence spectra using a 13-element germanium array detector. The results presented in this paper are the average of multiple scans. Data analyses were carried out as described previously (26–28). EXAFS, which were extracted by subtracting the background absorption, was converted to electron momentum  $k$  space, where  $k$  is a photoelectron wave vector. The resultant curve was then multiplied by  $k^3$  to equalize the oscillation amplitude in the  $k$  space. Curve fittings were performed using the non-

## Oxy Form of Guanylate Cyclase

linear least squares program EXCURV92 on the raw data weighted by  $k^3$ . Other details, including refinement of the data, are described elsewhere (26–28).

Resonance Raman spectra were measured with a JASCO NR-1800 spectrophotometer equipped with a cooled charge-coupled device detector (Princeton Instruments, Trenton, NJ). The excitation wavelength was 413.1 nm from a krypton ion laser (Coherent, Innova 90). The sample was directly mounted on an aluminum sample holder and frozen with liquid  $N_2$ . The sample holder was then inserted into the cryostat (Oxford DN1704), and the temperature of the sample was kept at 85 K with a temperature controller (Oxford ITC502).

**Stopped-flow Measurements**—The binding of alkyl isocyanides to the ferrous sGC was followed by a DX-18MV stopped-flow apparatus (Applied Photophysics, Leatherhead, UK). The anaerobic sGC solution was mixed with an anaerobic solution containing a desired amount of *t*-butyl or isopropyl isocyanide in the stopped-flow instrument at 20 °C. The reaction was performed under pseudo-first order conditions, and the rate constants were determined by fitting to a single exponential function using built-in software. The association rate constant ( $k_{on}$ ) and dissociation rate constant ( $k_{off}$ ) were determined from the slope and the *y* axis intercept, respectively, in the plot of the observed rates versus isocyanide concentrations.

**Activity Measurements**—End-point assays were performed in the cooling bath maintained at  $-7$  °C by a Eulabo F 13 temperature controller. The assay mixture contained 470  $\mu$ M GTP, 7 mM  $MgCl_2$ , 50 mM NaCl, 10% ethylene glycol, and an appropriate amount of the enzyme solution in 150  $\mu$ l of 40 mM TEA buffer. When desired, 104  $\mu$ M YC-1 or 37  $\mu$ M BAY41–2272 was added to the reaction mixture supplemented with 4% DMF to maintain the solubility of YC-1 or BAY41–2272. The mixtures were equilibrated in a septum-sealed anaerobic reaction vial with 2 atmospheres of  $O_2$  or  $N_2$ . Reactions were started by the addition of 1.5  $\mu$ M native or deuteroheme-substituted sGC and conducted at  $-7$  °C for 30 min. The reaction was terminated by the addition of 5  $\mu$ l of 30% acetic acid. The amount of cGMP formed was quantified by analysis on a C18 high performance liquid chromatography column equilibrated with 20 mM potassium phosphate buffer containing 10% methanol at a constant flow rate of 1 ml/min.

**Oxidation-Reduction (Redox) Potential Measurements**—Spectroelectrochemical apparatus originally designed by Tsumijima *et al.* (29) was modified to enable direct monitoring of the redox potential with a platinum indicator electrode. An anaerobic 1-cm path length cuvette was used with a septum-capped port for injection and a female ground glass joint at the top that fitted to a male joint of a micro combined electrode, EA 234 (Metrohm, Herisau, Switzerland). A platinum mesh electrode (52 mesh,  $8 \times 10$  mm) and platinum wire electrode (0.6-mm diameter) were also fixed on the inside walls of the cuvette to act as working and counter electrodes, respectively, in three-electrode potentiostat system. The combined electrode comprised a platinum indicator and  $Ag^+/AgCl$  reference electrode that was connected to a pH meter, model Accumet AR15 (Fisher), to directly monitor the electrode potentials. After the buffer solution containing mediators (1.6 ml) was introduced into the spectroelectrochemical cuvette, the com-

bined electrode was attached to the cuvette by fitting the joints, thereby making an air-tight seal. The solution was purged with purified  $N_2$  for 10 min. Then, the concentrated protein sample was introduced into the cuvette through the rubber septum cap. The cuvette was then placed in a temperature-controlled cell holder. The solution was constantly stirred with a magnetic stirrer during data collection. The desired redox levels of the protein sample were maintained by coulometric generation of mediator-titrant that was controlled by the three-electrode potentiostat system. The potential control by the three-electrode system was achieved by using a potentiostat, model HA-151A (Hokuto Denko Co., Tokyo, Japan). Redox potentials are quoted relative to the normal hydrogen electrode. The mediators used were 33  $\mu$ M  $Ru(NH_3)_6Cl_3$ , 33  $\mu$ M *p*-benzoquinone, 10  $\mu$ M toluylene blue, and 20  $\mu$ M 3'-chloroindophenol. Dithiothreitol included in the stored sGC solution was removed by passing through a Superdex 200HR column (GE Healthcare) to avoid undesired redox reactions.

**Reagents**—GTP, *t*-butyl isocyanide, and isopropyl isocyanide were purchased from Sigma. YC-1 was purchased from ALEXIS (San Diego, CA). Other chemicals, purchased from Wako Chemicals Co. (Tokyo, Japan), were of the highest commercial grade.

## RESULTS AND DISCUSSION

**Detection and Characterization of the Oxy Form at Low Temperature**—We observed that the yellowish-red-colored sGC preparation in the air-saturated buffer changed to brilliant red upon freezing in liquid  $N_2$ , suggesting formation of a low spin heme. We analyzed the temperature-dependent change by low temperature optical spectroscopy at 77 K. Under anaerobic conditions, in which dissolved  $O_2$  was removed by  $Na_2S_2O_4$ , the enzyme exhibited a spectrum corresponding to a high spin heme with the Soret band at  $\sim 430$  nm and a broad band centered at 560 nm in the visible region at 77 K (Fig. 1*a*). By contrast, the spectrum of sGC in air-saturated buffer (*i.e.* in the absence of  $Na_2S_2O_4$ ) at 77 K displayed well resolved  $\alpha$  and  $\beta$  bands at 543 and 577 nm, respectively, accompanied by blue shift of the Soret band to 421 nm (Fig. 1*b*). Such distinct  $O_2$ -dependent spectral changes were not observed at ambient temperature (298 K) where sGC exhibited a spectrum typical of ferrous high spin heme both in the presence and absence of  $Na_2S_2O_4$  at 298 K (*inset* of Fig. 1). The new species did not exhibit EPR signals assignable to ferric heme iron at either 15 and 5K. These findings together indicate that the species is in a ferrous low spin state and may be assigned to an oxy form of sGC based on the spectral similarities with that of oxyhemoglobin and the absolute requirement of  $O_2$  for its formation. Hereafter, we interpret experimental results by assuming that the ferrous heme iron in the enzyme is capable of binding  $O_2$  like the cobalt-substituted enzyme.

Although we have no available data to argue the mechanism of the formation, it is clear that the oxy form is produced in a course of freezing. The putative oxy form exhibited a somewhat broad Soret band with an obvious shoulder at around 430 nm and with a significant red-shifted Soret peak position in comparison with the Soret peak (417 nm) of oxyhemoglobin (Fig. 1*b*). These spectral properties suggested that the formation of

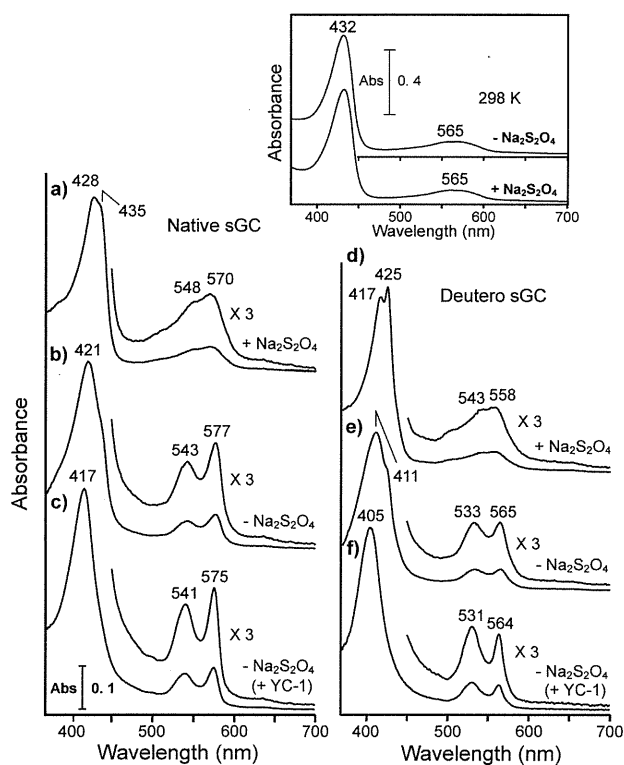


**FIGURE 1. Low temperature optical spectra of sGC.** Optical spectra of native sGC (7.1  $\mu\text{M}$ ) at 77 K are summarized in the left panel. Trace a, native ferrous sGC in an anaerobic buffer, in which dissolved  $\text{O}_2$  was removed by the addition of  $\text{Na}_2\text{S}_2\text{O}_4$ , was frozen at 77 K, and then the spectrum was recorded. Trace b, shown is the spectrum of native ferrous sGC in the air-saturated buffer. Trace c, shown is native ferrous sGC in the air-saturated buffer containing YC-1 (104  $\mu\text{M}$ ). Spectra of deuterioheme-substituted enzyme at 77 K are shown in the right panel. Trace d, shown is deuterioheme-substituted sGC in the anaerobic buffer with  $\text{Na}_2\text{S}_2\text{O}_4$ . Trace e, shown is deuterioheme-substituted sGC in the air-saturated buffer. Trace f, shown is deuterioheme-substituted sGC in the air-saturated buffer containing YC-1 (104  $\mu\text{M}$ ). The buffer used was 40 mM TEA, pH 7.5, containing 5% (v/v) ethylene glycol and 50 mM NaCl. In traces c and f, 4% (v/v) DMF was supplemented in the above buffer to maintain the solubility of YC-1. The addition of DMF did not change the spectral features both in anaerobic and aerobic conditions. In the inset, optical spectra of native sGC at 298 K in the presence and absence of  $\text{Na}_2\text{S}_2\text{O}_4$  are shown.

the oxy form was incomplete because of the low affinity of the enzyme-heme for  $\text{O}_2$ . Likewise, complete formation of the oxy form was not observed for deuterioheme-substituted sGC despite the large increase in  $\text{O}_2$  affinity by heme substitution as shown for myoglobin and hemoglobin (30, 31) (Fig. 1e). Therefore, it is unlikely that the incomplete  $\text{O}_2$  occupation is due to the low  $\text{O}_2$  affinity of the enzyme-heme. The complete formation of the oxy form was achieved by the addition of YC-1, as shown by a blue shift of the Soret band and intensified  $\alpha$  and  $\beta$  bands (Fig. 1, c and f). These findings seem to indicate that YC-1 converts the  $\text{O}_2$ -insensitive conformation to an  $\text{O}_2$  binding conformation.

We attempted to detect  $\text{O}_2$  ligation at the axial position of the heme by resonance Raman spectroscopy at 80 K. Oxyhemoglobin used as control exhibited a  $\nu_4$  Raman band at  $1380\text{ cm}^{-1}$  and a  $\nu_3$  band at  $1511\text{ cm}^{-1}$  characteristic of 6-coordinate low spin oxy heme (data not shown). Unlike hemoglobin, sGC frozen at 80K in the air-saturated buffer exhibited only 5-coordi-

nate high spin bands at  $1358$  and  $1476\text{ cm}^{-1}$  without showing any 6-coordinate low spin Raman bands either in the presence and absence of YC-1 (data not shown). We interpreted these spectral characteristics to be caused by conversion of the 6-coordinate oxy heme to 5-coordinate heme as a result of photodissociation of the bound  $\text{O}_2$ . Thus, it was not possible to identify  $\text{O}_2$  ligation by resonance Raman spectroscopy. Next, we tried to detect ligation of  $\text{O}_2$  at the metal center using  $\text{Co}^{2+}$ -protoporphyrin-substituted enzyme.

We have reported that the  $\text{Co}^{2+}$ -protoporphyrin-substituted sGC has a weak  $\text{Co}^{2+}$ -His bond and produces 5-coordinate NO complex like the native sGC (14). The present experiments further established that the metal substitution has no effect on the structure as well as catalytic properties of the enzyme, because there are no significant differences in the catalytic and the nucleotide binding properties and in the subunit structure and protein surface charges between the native and the Co-substituted enzymes (supplemental Figs. 1 and 2).

The optical spectrum of  $\text{Co}^{2+}$ -proto sGC measured at 77 K in the presence of  $\text{Na}_2\text{S}_2\text{O}_4$  showed a Soret band at 403 nm and 524- and 557-nm bands in the visible region (Fig. 2A). When frozen in the air-saturated buffer, the 557-nm band of  $\text{Co}^{2+}$ -protoporphyrin sGC was significantly decreased in intensity with an appearance of a new band at 574-nm and a significant red shift of the Soret band (Fig. 2B). The addition of YC-1 augmented the  $\text{O}_2$ -dependent spectral change (Fig. 2C). In the  $\text{O}_2$ -saturated buffer supplemented with YC-1, the spectrum converted to that of a single species with 420, 542, and 574 bands (Fig. 2D). These spectral features essentially agree with those of oxy Co-proto myoglobin (32). The species showed a free radical type EPR signal with hyperfine structure at  $g_1 \sim 2.08$ , which results from a coupling of unpaired electron to the Co nucleus (inset of Fig. 2). This is conclusive evidence for the formation of the oxy form ( $\text{Co}^{3+} - \text{O}_2^-$ ) of cobalt-porphyrin (33, 34).  $\text{Co}^{2+}$ -mesoporphyrin sGC also exhibited similar  $\text{O}_2$ -dependent spectral changes (supplemental Fig. 3).

The coordination structures of the enzyme-heme in the unliganded,  $\text{O}_2$ -bound, and CO-bound states were examined by the iron K-edge EXAFS. The  $k^3$ -weighted EXAFS and the corresponding Fourier transforms are summarized in Fig. 3. To fit the experimental data, His, His and  $\text{O}_2$ , and His and CO were employed as the axial ligands for the ferrous, the  $\text{O}_2$ -bound, and the CO-bound hemes, respectively. The atomic coordination of corresponding myoglobin derivatives were employed as a starting model of the curve fitting. The structural parameters that satisfy the raw data by these approaches are summarized in Table 1. EXAFS of the unliganded ferrous sGC, obtained in the presence of  $\text{Na}_2\text{S}_2\text{O}_4$  (spectrum A in the left panel Fig. 3), was similar to that of deoxymyoglobin (28, 35). The iron in the unliganded ferrous sGC was displaced relative to the heme plane ( $\text{Fe}^{2+}$ -Ct, distance between  $\text{Fe}^{2+}$  and porphyrin plane center) by  $0.56\text{ \AA}$ , like deoxymyoglobin (Table 1). The displacement is characteristic of high spin heme, because the high spin heme iron cannot be forced into the porphyrin plane due to the large covalent radius of high spin iron.

It is generally accepted that the  $\text{Fe}^{2+}$ -His bond strength of sGC is weaker than that of myoglobin due to strain at the heme center (13, 14, 17, 36). Although the difference in the  $\text{Fe}^{2+}$ -His

## Oxy Form of Guanylate Cyclase

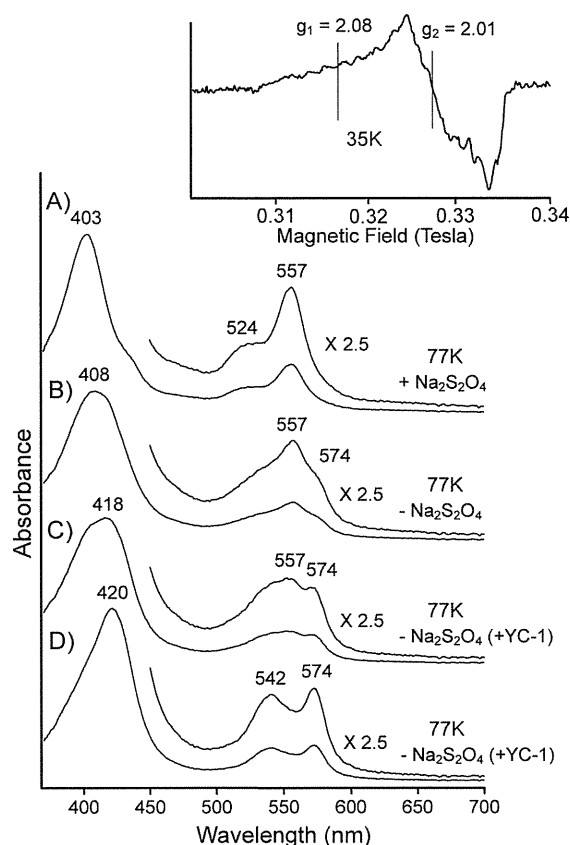


**FIGURE 2. Low temperature optical spectra of cobalt protoporphyrin-substituted sGC.** Trace A,  $\text{Co}^{2+}$ -protoporphyrin-substituted sGC in the anaerobic buffer in which dissolved  $\text{O}_2$  was removed by  $\text{Na}_2\text{S}_2\text{O}_4$  was frozen at 77 K, and then the spectrum was taken. Trace B, the spectrum of  $\text{Co}^{2+}$ -protoporphyrin-substituted sGC in the air-saturated buffer is shown. Trace C, the spectrum of  $\text{Co}^{2+}$ -protoporphyrin sGC in the air-saturated buffer containing YC-1 (104  $\mu\text{M}$ ) is shown. Trace D, the spectrum of  $\text{Co}^{2+}$ -protoporphyrin-substituted sGC in the  $\text{O}_2$ -saturated buffer containing YC-1 (104  $\mu\text{M}$ ) is shown. The buffer used was 40 mM TEA, pH 7.5, containing 5% (v/v) ethylene glycol and 50 mM NaCl. *Inset*, X-band (9.22 GHz) EPR spectrum of  $\text{Co}^{2+}$ -protoporphyrin-substituted sGC in the  $\text{O}_2$ -saturated buffer was taken at 35 K and by 100 K Hz field modulation with 1-millitesla width.

bond strength between sGC and myoglobin was thought to be reflected in the  $\text{Fe}^{2+}$ -His bond distance, the  $\text{Fe}^{2+}$ -His bond distance observed in unliganded sGC essentially agreed with that of deoxymyoglobin (Table 1). The discrepancy may be explained by the tilting of the  $\text{Fe}^{2+}$ -imidazole nitrogen bond from the heme normal, because such a distortion also weakens the  $\text{Fe}^{2+}$ -His bond strength probably by decreasing  $\pi$ -bond interaction between iron  $d\pi$ -orbital and imidazole nitrogen  $p\pi$ -orbital.

EXAFS of sGC in the presence and absence of  $\text{O}_2$  were different, indicating binding of exogenous ligand at the axial position (spectrum B in the left panel of Fig. 3). Placing  $\text{O}_2$  at the 6th position of the heme using the parameters listed in Table 1, the heme iron was found to still bind the proximal His with a bond distance of 2.13 Å (Table 1). The iron displacement from the heme plane was much reduced upon placing  $\text{O}_2$  on the heme iron (0.09 Å) (Table 1). These results showed that the proximal His moved toward the heme plane along with the movement of

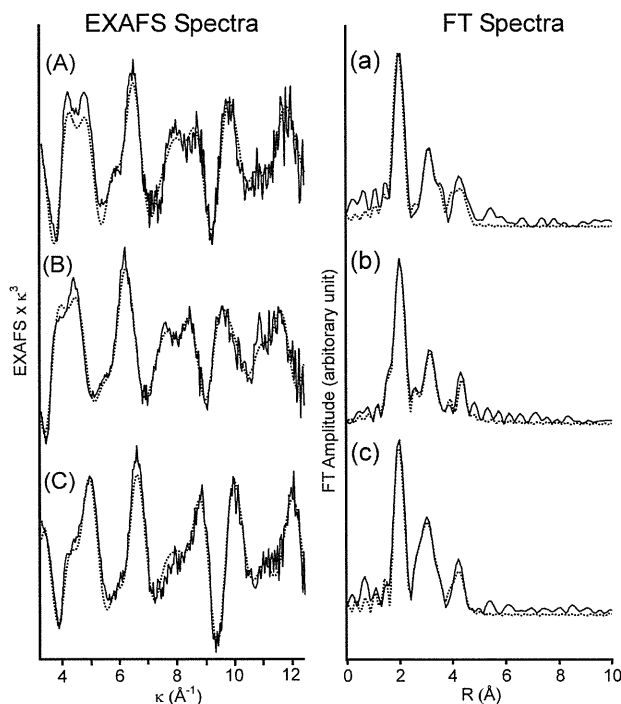


**FIGURE 3.  $k^3$  EXAFS spectra and their Fourier transforms of sGC.** EXAFS spectra and their Fourier transforms (FT) were depicted in the left and the right panels, respectively. Traces A and a were in the presence of  $\text{Na}_2\text{S}_2\text{O}_4$ . Traces B and b were in the presence of  $\text{O}_2$ . Traces C and c were in the presence of CO. The buffer used was 40 mM TEA, pH 7.5, containing 5% (v/v) ethylene glycol and 50 mM NaCl. The enzyme concentration was 470  $\mu\text{M}$  as here. The solid lines indicate the observed EXAFS and Fourier transforms, and the dashed lines depicted simulation curves. The analyses incorporate multiple scattering from the outer shell atoms of the porphyrin ring and axial ligand molecules. Other details including refinement of data are described elsewhere (26–28).

**TABLE 1**  
**Iron-ligand distances for soluble guanylate cyclase and myoglobin in their unliganded,  $\text{O}_2$ , and CO forms estimated by EXAFS**

The parameters used to simulate the K-edge EXAFS are principally the same as those by Binsted *et al.* (26). Distances (R) and Debye-Waller terms of the ligand atom coordinating iron ( $2\sigma^2$ ) are included in the table. The abbreviations used are:  $\text{Fe}^{2+}$ -Ct, distance of iron from the porphyrin plane center (magnitude of iron displacement);  $\text{Fe}^{2+}$ -Npyr, bond distance between iron and porphyrin nitrogen atom;  $\text{Fe}^{2+}$ -Nim, bond distance between iron and proximal His imidazole nitrogen atom;  $\text{Fe}^{2+}$ -L, bond distance between iron and sixth ligand.

$\text{Fe}^{2+}$ -ligand site	$\text{Fe}^{2+}$		$\text{Fe}^{2+}$ - $\text{O}_2$		$\text{Fe}^{2+}$ -CO	
	R	$2\sigma^2$	R	$2\sigma^2$	R	$2\sigma^2$
	Å	Å <sup>2</sup>	Å	Å <sup>2</sup>	Å	Å <sup>2</sup>
<b>sGC</b>						
$\text{Fe}^{2+}$ -Ct	0.56		0.09		0.13	
$\text{Fe}^{2+}$ -Npyr	2.09	0.004	2.09	0.002	2.05	0.003
$\text{Fe}^{2+}$ -Nim	2.10	0.005	2.13	0.006	2.05	0.002
$\text{Fe}^{2+}$ -L			1.89	0.004	1.85	0.004
<b>Myoglobin</b>						
$\text{Fe}^{2+}$ -Ct	0.48		0.00		0.02	
$\text{Fe}^{2+}$ -Npyr	2.05	0.004	1.99	0.002	1.99	0.004
$\text{Fe}^{2+}$ -Nim	2.11	0.003	2.02	0.005	2.09	0.003
$\text{Fe}^{2+}$ -L			1.85	0.004	1.81	0.003

the heme iron to produce the 6-coordinate oxy form, and therefore, the low affinity for  $\text{O}_2$  may be not caused by cleavage of the  $\text{Fe}^{2+}$ -His bond. In the case of the CO complex, iron displacement of the CO complex was 0.13 Å. The value was somewhat larger than that of the corresponding derivative of myoglobin



## Oxy Form of Guanylate Cyclase

(Fig. 3 and Table 1), but these values fall in the range of a low spin iron.

To characterize the distal heme pocket structure, we focused on the bond distance and angle of  $\text{Fe}^{2+}$ -ligand coordination, which were obtained with multiple scattering analyses of a limited narrow  $k$  range EXAFS ( $3\text{--}13 \text{ \AA}^{-1}$ ) (28). The geometries of sGC-ligand complexes are  $\text{Fe}^{2+}$ - $\text{O}_2$  bond distance =  $1.89 \text{ \AA}$  and  $\text{Fe}^{2+}$ -O-O bond angle =  $120^\circ$  for the oxy form, and  $\text{Fe}^{2+}$ -CO bond distance =  $1.85 \text{ \AA}$  and  $\text{Fe}^{2+}$ -C-O bond angle =  $171^\circ$  for the CO form. The coordination geometry for myoglobin obtained by the present curve fitting procedure was  $1.85 \text{ \AA}$  (bond distance) and  $104^\circ$  (bond angle) for the  $\text{O}_2$  form and  $1.81 \text{ \AA}$  and  $149^\circ$  for the CO form. These values for myoglobin essentially agreed with those obtained by x-ray crystallographic analyses (37, 38). The present method for data analyses is useful for estimating iron-ligand geometry, although there is uncertainty in bond angle determination of  $\sim 10^\circ$ , including absolute and fitting errors (28, 39). Therefore, the EXAFS studies on sGC indicate that the CO moiety of the  $\text{Fe}^{2+}$ -CO unit binds to the heme iron with a nearly linear geometry. Such geometry implies no steric protein effect on the distal side of the heme. Conversely,  $\text{O}_2$  seems to accommodate on the distal pocket with intrinsically bent  $\text{Fe}^{2+}$ - $\text{O}_2$  structure.

To establish whether the ligation of  $\text{O}_2$  affects the cyclase activity, we attempted to detect the oxy form under fluid conditions. In these experiments the formation of the oxy form was followed by the difference spectra against the spectrum in the presence of  $\text{N}_2$ . At  $-7^\circ\text{C}$ , the difference spectra exhibited a 410-nm peak and a 434-nm trough in the Soret region and peaks at 539 and 578 nm in the visible region (trace a in Fig. 4A). The intensity of the 410-nm peak in the difference spectrum significantly increased in the presence of YC-1 (trace b in Fig. 4A). The spectral species formed under an atmosphere of  $\text{O}_2$  was assignable to an oxy form, because these peak and trough positions were essentially the same as those in the difference spectrum at 77 K (Fig. 4B). The amount of oxy form produced at  $-7^\circ\text{C}$  was estimated to be only 3% of total protein even in the presence of YC-1, based on the pure oxy form obtained arithmetically as described below. The formation of oxy form was temperature-dependent and significantly decreased upon raising the temperature to  $3^\circ\text{C}$  (data not shown).

Deuteroheme substitution has been known to increase  $\text{O}_2$  affinity (30, 31). As anticipated, the degree of oxy form formed at  $-7^\circ\text{C}$  was greater than that of the native enzyme (trace c in Fig. 4A). Nevertheless, the yield of oxy form for the deuteroheme-substituted enzyme was still only  $\sim 4\%$ . YC-1 significantly increased the formation of the oxy form in the deuteroheme-substituted enzyme to approximately  $\sim 7\%$  of total protein (trace d in Fig. 4A).

The effect of  $\text{O}_2$  on cyclase activity was examined in the presence of YC-1 at  $-7^\circ\text{C}$  (Fig. 4C). The addition of NO resulted in 120-fold activation of the native enzyme, whereas the presence of  $\text{O}_2$  did not appear to enhance the cyclase activity in the absence and presence of YC-1. Similar results were also observed for the deuteroheme-substituted enzyme, where the presence of  $\text{O}_2$  did not enhance the cyclase activity of the substituted-enzyme in the presence of YC-1 and its derivative, BAY 41-2272 (3-(5'-hydroxymethyl-3'-furyl)-1-benzylindazole)

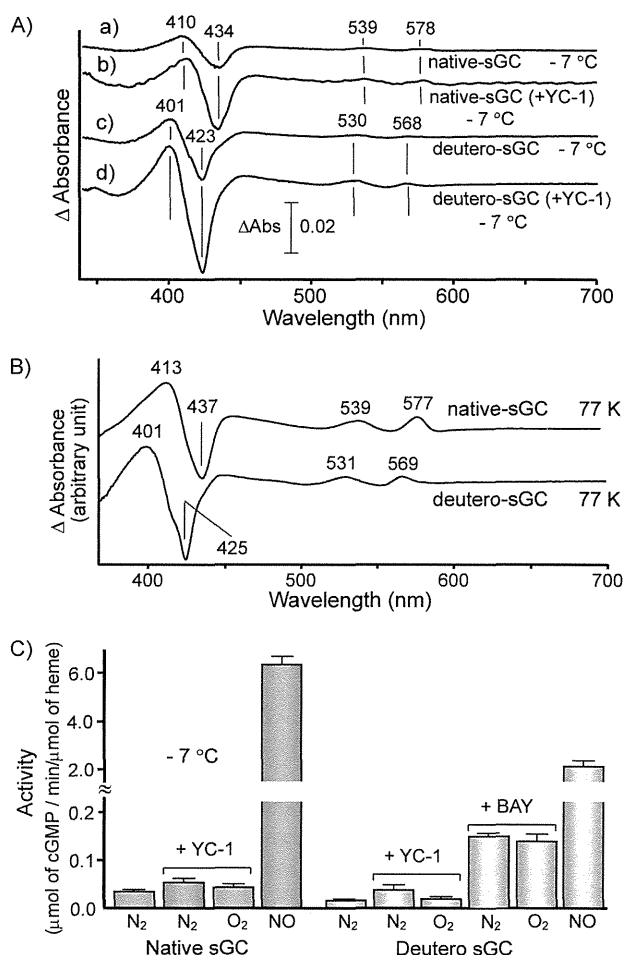


**FIGURE 4. Difference spectra of native and deuteroheme-substituted sGC between anaerobic and aerobic conditions and their cyclase activities at low temperature.** In A, the difference spectra between  $\text{O}_2$  and  $\text{N}_2$  atmosphere under fluid conditions were summarized. The enzyme samples and temperature are indicated in the figure. The enzyme concentrations were  $15.1 \mu\text{M}$  in both the native and the substituted enzymes. Traces a and b were for native sGC, and traces c and d were for deuteroheme-substituted sGC. In B, the difference spectra between  $\text{O}_2$  and  $\text{N}_2$  atmosphere under frozen conditions at 77 K are illustrated. The difference spectra shown were obtained by subtracting the spectrum under  $\text{N}_2$  atmosphere from that under  $\text{O}_2$  atmosphere. In C, activities of native and deuteroheme-substituted enzymes were assayed in 40 mM TEA, pH 7.5, containing 10% ethylene glycol, 50 mM NaCl, 7 mM  $\text{MgCl}_2$ , and 0.47 mM GTP. When the addition of YC-1 ( $104 \mu\text{M}$ ) or BAY 41-2272 ( $40 \mu\text{M}$ ) was desired, 4% DMF was supplemented to the above buffer to maintain the solubility. The effect of DMF on the basal and NO-stimulated activities was negligible under the experimental conditions.

(Fig. 4C). In this connection it is interesting to note that the cyclase activity catalyzed by Gcy-88E from *Drosophila* was not stimulated by CO, NO, and  $\text{O}_2$  (40). This enzyme formed stable 6-coordinate NO and  $\text{O}_2$  complex, unlike typical sGC. These results together with the present data suggest that the ligand-dependent stimulation may be closely coupled with the  $\text{Fe}^{2+}$ -His bond strength, although the detailed mechanism remains to be elucidated.

To ask whether the exogenous heme-ligand can prevent  $\text{O}_2$  binding to the enzyme-heme, we examined the inhibitory effect on the  $\text{O}_2$  binding. As shown in Fig. 5A, the  $\text{O}_2$ -dependent spectral change in the presence of BAY 41-2272 yielded the

## Oxy Form of Guanylate Cyclase

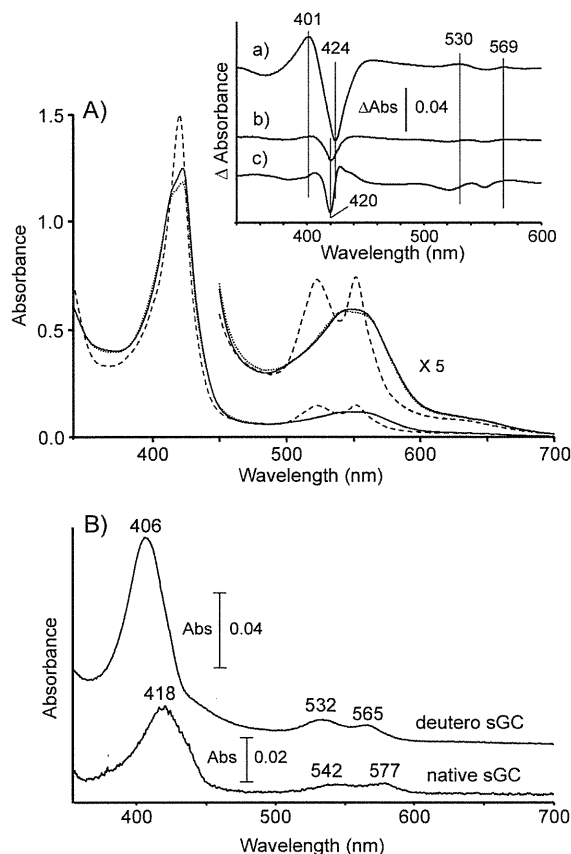


**FIGURE 5. The effect of isocyanide on the O<sub>2</sub> binding and the spectra of the complete oxy form.** In A, the optical spectra of deuteroheme-substituted sGC in the presence of BAY 41-2272 were illustrated. The spectra shown by a *solid* and a *dotted line* are the spectrum of the ferrous enzyme in the N<sub>2</sub>-saturated and in the O<sub>2</sub>-saturated buffer, respectively. The spectrum shown by the *broken line* was that in the presence of isopropyl isocyanide (170 μM). The buffer used was 40 mM TEA buffer, pH 7.5, containing 10% ethylene glycol, 50 mM NaCl, 4% DMF, and 37 μM BAY 41-2272. The difference spectra were summarized in the *inset*, where *trace a* is a difference spectrum by subtracting the spectrum in the N<sub>2</sub>-saturated buffer from that in the O<sub>2</sub>-saturated buffer, and *trace b* was obtained by subtracting the spectrum in the N<sub>2</sub> buffer from that in the O<sub>2</sub> buffer, of which buffers contained isopropyl isocyanide (170 μM). *Trace c* is the difference spectrum by subtracting the spectrum of the isopropyl isocyanide adduct from that of the ferrous enzyme, which is illustrated in the 1/10 scale. In B, the spectrum of the complete oxy form was arithmetically obtained by subtracting the ferrous spectrum multiplied by a factor from the spectrum in the O<sub>2</sub>-saturated buffer. The data used for the native enzyme were the absolute spectra (in N<sub>2</sub> and O<sub>2</sub>) used to generate *trace b* in Fig. 4A and for the deuteroheme-substituted enzyme the spectra in Fig. 5A. The subtractions of the ferrous enzyme multiplied by 0.97 and 0.89 could satisfactorily eliminate the residual ferrous enzyme for the native and the deuteroheme enzymes, respectively.

largest change observed so far (compare the *solid line* with the *dotted line*). In contrast, the O<sub>2</sub>-dependent spectral change was noted to be much reduced when isopropyl isocyanide was included in the mixture (compare *trace a* with *trace b* in the *inset* of Fig. 5A). The difference spectrum (*trace b*) does not agree with *trace a* in the entire spectral region. Although the *trace b* displayed the trough at 420 nm similar to that of *trace c*, the bandwidth of *trace b* was much larger than that of *trace c*, suggesting the displacement of the bound isocyanide by O<sub>2</sub>. The nearly identical result was also observed for native sGC in the reaction of the *t*-butyl isocyanide adduct with O<sub>2</sub> (data not

shown). These spectral features agreed with the view that isocyanide competed with the same site as O<sub>2</sub>.

The spectrum of the complete oxy form could be arithmetically obtained by subtracting the ferrous-enzyme spectrum multiplied by a factor from the spectrum in the O<sub>2</sub>-saturated buffer. In the presence of YC-1 and BAY 41-2272, as shown in Fig. 5A, the subtractions of the ferrous enzyme multiplied by 0.97 and 0.89 could satisfactorily eliminate the residual ferrous enzyme for the native and the deuteroheme enzyme, respectively. The resultant arithmetic spectra (Fig. 5B) agree with those of the oxy form obtained at 77K (Fig. 1). On the basis of these results together with EXAFS and other optical spectral studies described in this paper, we finally conclude that the heme in sGC is capable of binding O<sub>2</sub>.

**Protein Effects on Ligand Binding**—Using the systematic kinetic data, Mims *et al.* (41) assessed the protein effects on the ligand binding of myoglobin. The effects are summarized as (i) distal steric hindrance to restrict the approach of the ligand to its final position and (ii) a protein proximal effect that controls successive bond formation of the iron with ligand on the distal side. When the bond between iron and ligand (such as O<sub>2</sub>) is generated, the distal His residue forms a hydrogen bond with the bound O<sub>2</sub> to stabilize the O<sub>2</sub> complex. These mechanisms, which were originally formulated for myoglobin, provide key clues in understanding the ligand binding of other hemoproteins.

We have assessed the distal steric protein effect by analyzing the reaction of the ferrous heme iron with alkyl isocyanides. As shown in Fig. 6A, careful titration with *t*-butyl isocyanide showed that the unliganded ferrous sGC converted to the isocyanide adduct through one set of isosbestic points. The binding of isopropyl isocyanide also yielded nearly identical species (data not shown). The optical spectra of these alkyl isocyanide adducts were essentially the same as those of the corresponding isocyanide adducts of myoglobin, demonstrating that the isocyanide adducts of sGC were in a six-coordinate low spin state (42). The dissociation constants ( $K_d$ ) calculated were 46 and 90 μM for *t*-butyl isocyanide and isopropyl isocyanide (*inset* of Fig. 6), respectively, indicating that the affinity for *t*-butyl isocyanide is significantly higher by comparison to that for isopropyl isocyanide. In general, the affinities of isocyanide for the hemoproteins decreased with increasing size of alkyl group in the isocyanide molecule (41). In contrast, sGC exhibited a higher affinity for isocyanide with a larger alkyl group. The anomalous property has also been noted for human hemoxygenase (43). The association rates of isocyanides with the ferrous sGC decreased with increasing size of alkyl group in the isocyanide molecule. The rates are 10-fold faster than the formation of the corresponding isocyanide adducts of myoglobin (Fig. 6B and Table 2) and nearly equivalent to those of leghemoglobin (44), which are the highest among the globin family. Taking into consideration these findings, we propose that there is no substantial resistance to the binding of bulky isocyanides with sGC, in contrast to myoglobin, supporting the previous result (45).

In accordance with a previous report (22), sGC binds CO with an association rate constant of  $3.6 \times 10^4 \text{ M}^{-1} \text{ s}^{-1}$ , which is particularly slow among 5-coordinate high spin hemoproteins (Table 2). The most striking feature is that the association rate

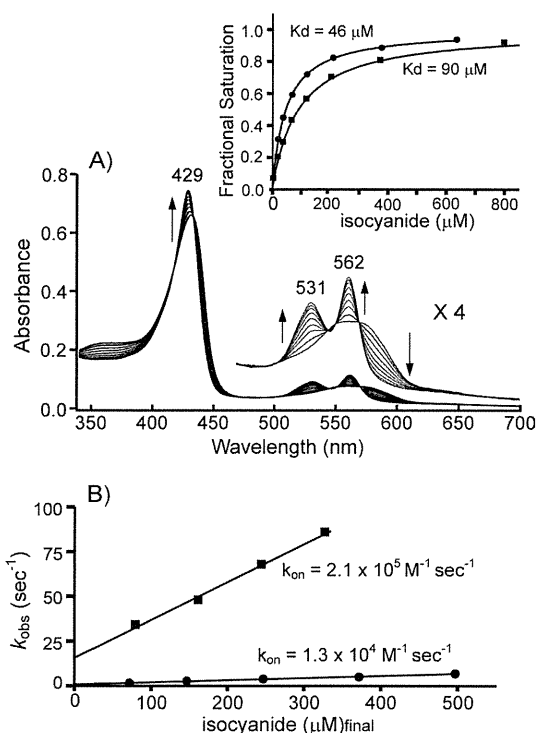


**FIGURE 6. Equilibrium binding and kinetic analyses of alkyl isocyanide binding.** *A*, shown are changes in the absorbance spectra of sGC during titration with *t*-butyl isocyanide. *B*,  $k_{\text{obs}}$  values obtained from stopped-flow traces were plotted against the final concentration of isocyanide after mixing. Closed circles (●) are data from *t*-butyl isocyanide, and closed squares (■) are data from isopropyl isocyanide. In the *inset*, isocyanide binding curves are plotted as the fractional saturation *versus* the effective concentration of isocyanide. *Solid lines* depicted simulated lines obtained by nonlinear regression analyses. Equilibrium and kinetic binding experiments were done at 20 °C. Other details are described under "Experimental Procedures."

**TABLE 2**

Ligand binding properties of soluble guanylate cyclase, sperm whale myoglobin, and soybean leghemoglobin

	$K_d$ $\mu\text{M}$	$k_{\text{on}}$ $\text{M}^{-1} \text{s}^{-1}$	$K_{\text{off}}$ $\text{s}^{-1}$	Reference
<b>Soluble guanylate cyclase</b>				
CO	298 <sup>a</sup>	$3.6 \times 10^4$	10.7	This study
Isopropyl isocyanide	90 (81 <sup>a</sup> )	$2.0 \times 10^5$	16.1	This study
<i>t</i> -Butyl isocyanide	48 (61 <sup>a</sup> )	$1.3 \times 10^4$	0.80	This study
<b>Sperm whale myoglobin</b>				
CO	0.03 <sup>a</sup>	$5.0 \times 10^5$	0.015	41
Isopropyl isocyanide	73 (87 <sup>a</sup> )	$7.5 \times 10^3$	0.65	This study
<i>t</i> -Butyl isocyanide	836 (803 <sup>a</sup> )	$1.5 \times 10^3$	1.20	This study
<b>Soybean leghemoglobin</b>				
CO	0.0013 <sup>a</sup>	$1.3 \times 10^7$	0.016	44
Isopropyl isocyanide	0.0073 <sup>a</sup>	$4.1 \times 10^5$	0.0030	44
<i>t</i> -Butyl isocyanide	0.082 <sup>a</sup>	$2.2 \times 10^4$	0.0018	44

<sup>a</sup> Calculated as  $k_{\text{off}}/k_{\text{on}}$ .

for isopropyl isocyanide was approximately one order of magnitude faster than that for CO binding, irrespective of the larger size of the isocyanide by comparison to CO (Table 2). These findings strongly suggest that sGC permits easy access for small ligands, such as CO and O<sub>2</sub>, to the coordination position. Therefore, the formation of the coordinate bond dominates the kinetics of association, accentuating the significance of the proximal protein effect.

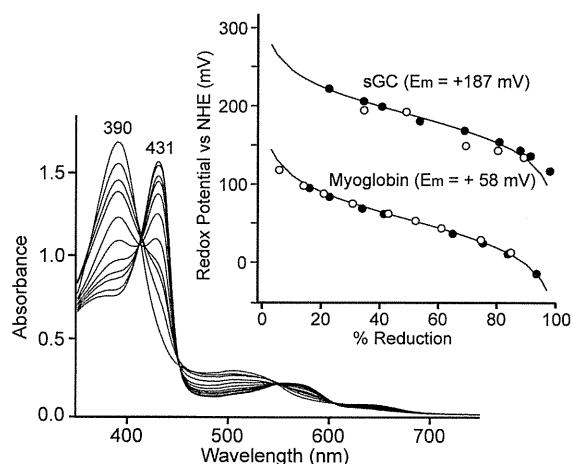


**FIGURE 7. Anaerobic redox titration of sGC.** The reaction mixture contained 15  $\mu\text{M}$  of sGC or sperm whale myoglobin and a mixture of mediators in 50 mM Hepes buffer at pH 7.5 containing 50 mM KCl and 5% ethylene glycol. The final volume was 1.6 ml. The cuvette was kept under an anaerobic atmosphere of N<sub>2</sub> at 20 °C. The desired redox levels were maintained by coulometric generation of mediator-titrant, of which potentials were controlled by a three-electrode system as described in under "Experimental Procedures." After the reaction was achieved to redox equilibrium, spectra were recorded. Redox potentials were determined by both the reductive (○) and oxidative (●) titrations, in which the potentials were directly monitored by a combined micro-electrode. In the *inset*, redox potentials were plotted against the degree of reduction. *Solid lines* denote the theoretical lines calculated according to Nernst equation with  $n = 1$ . Other details were described under "Experimental Procedures." Mediators used were 17  $\mu\text{M}$  pyocyanine, 2  $\mu\text{M}$  2,6-dichloroindophenol, 6.6  $\mu\text{M}$  toluylene blue, and 33  $\mu\text{M}$  Ru(NH<sub>3</sub>)<sub>6</sub>Cl<sub>3</sub> for myoglobin and 33  $\mu\text{M}$  *p*-benzoquinone, 33  $\mu\text{M}$  Ru(NH<sub>3</sub>)<sub>6</sub>Cl<sub>3</sub>, 10  $\mu\text{M}$  toluylene blue, and 20  $\mu\text{M}$  3'-chloroindophenol for sGC. NHE denotes Normal Hydrogen Electrode.

Based on quantum mechanical and molecular mechanical analyses, it was proposed that the degree of electron density on the heme iron might be controlled by the protein proximal effect (46). This effect on the proximal side modulates the Fe<sup>2+</sup>-ligand bond formation on the distal side. For instance, when the Fe<sup>2+</sup>-proximal His bond is weakened by strain imposed on the bond, the electron density on the heme iron is reduced relative to that of the Fe<sup>2+</sup>-His bond without strain. This might reduce the electron donation from the iron to ligand such as O<sub>2</sub>, resulting in the weakening of the Fe<sup>2+</sup>-O<sub>2</sub> bond strength (46). Thus, a weak Fe<sup>2+</sup>-His bond correlates with a weak Fe<sup>2+</sup>-O<sub>2</sub> bond and vice versa. Such a protein effect, referred to as a positive *trans* effect, accounts for the unique character of the CO and O<sub>2</sub> binding characteristics of the iron-porphyrin complexes (47–50). The proximal effect derived by strain on the Fe<sup>2+</sup>-His bond probably affects redox potential of the heme, because the decrease in electron density at the ferrous heme makes it more difficult to remove an electron (51). For example, T-state hemoglobin with a more strained Fe<sup>2+</sup>-His bond and lower O<sub>2</sub> affinity relative to R-state hemoglobin exhibited significantly higher midpoint potentials of the heme than R-state hemoglobin (52). The redox potential measurements of sperm whale myoglobin and sGC indicated that the electrochemical titration curves fitted to a Nernst equation with  $n = 1$  in both hemoproteins (Fig. 7). The ferric-ferrous couple of myoglobin gave the midpoint potential of +58 mV, in reasonable agreement with the reported value. The midpoint potential of sGC, +187 mV, was considerably higher than that

## Oxy Form of Guanylate Cyclase

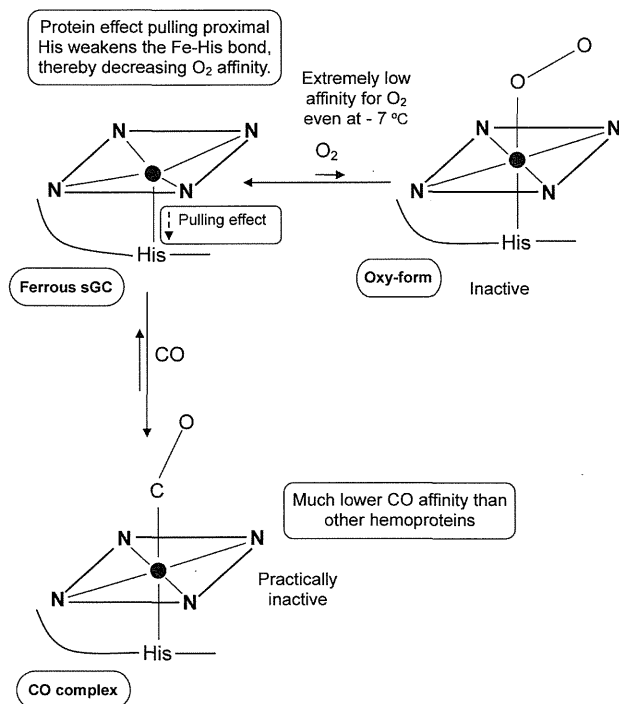


**FIGURE 8. Model proposed for bindings of the ferrous sGC with O<sub>2</sub> and CO.** The heme coordination structures were depicted based on EXAFS data (Table 1). Closed circles illustrated in the center of heme denote ferrous iron atom. The weak Fe<sup>2+</sup>-His bond in the ferrous enzyme may decrease charge density on the heme iron, thereby decreasing the O<sub>2</sub> affinity and elevating the redox potential of the heme.

of myoglobin. It should be noted that the measured value was the most positive among high spin protoheme-containing hemoproteins, presumably because the electron density of the heme in sGC is significantly reduced by the protein proximal effect. Based on the above considerations and EXAFS data, the significance of the proximal protein effect on the ligand binding was noted as summarized in Fig. 8.

In summary, we have detected and characterized the oxy form of sGC. To assess the crucial determinant(s) for the low O<sub>2</sub> affinity of sGC, we have analyzed the coordination structure by EXAFS. Our results indicate that the low affinity for O<sub>2</sub> is not caused by cleavage of the Fe<sup>2+</sup>-proximal His bond. Among protein effects to regulate the reactivity of heme, the distal steric hindrance could be excluded based on the kinetic studies. The critical factor that may contribute to the low O<sub>2</sub> affinity is the protein proximal effect, a regulatory effect caused by the weak Fe<sup>2+</sup>-proximal His bond. Measurement of the midpoint potential of the heme also highlights the significance of the protein proximal effect in terms of the unique low O<sub>2</sub> affinity of sGC. Based on the findings described in this paper, we propose that the weak Fe<sup>2+</sup>-proximal His bond is a key factor in regulating the reactivity of the heme in sGC along with the hydrogen bond interaction in the distal pocket, which was identified previously by mutational analysis (20).

## REFERENCES

1. Furchgott, R. F., and Zawadzki, J. V. (1980) *Nature* **288**, 373–376
2. Ignarro, L. J., and Kadowitz, P. J. (1985) *Annu. Rev. Pharmacol. Toxicol.* **25**,

- 171–191
3. Waldman, S. A., and Murad, F. (1987) *Pharmacol. Rev.* **39**, 163–196
4. Garthwaite, J., Charles, S. L., and Chess-Williams, R. (1988) *Nature* **336**, 385–388
5. Bredt, D. S., and Snyder, S. H. (1989) *Proc. Natl. Acad. Sci. U.S.A.* **86**, 9030–9033
6. Moncada, S., and Higgs, E. A. (1991) *Eur. J. Clin. Invest.* **21**, 361–374
7. Verma, A., Hirsch, D. J., Glatt, C. E., Ronnett, G. V., and Snyder, S. H. (1993) *Science* **259**, 381–384
8. Kamisaki, Y., Saheki, S., Nakane, M., Palmieri, J. A., Kuno, T., Chang, B. Y., Waldman, S. A., and Murad, F. (1986) *J. Biol. Chem.* **261**, 7236–7241
9. Stone, J. R., and Marletta, M. A. (1994) *Biochemistry* **33**, 5636–5640
10. Humbert, P., Niroomand, F., Fischer, G., Mayer, B., Koesling, D., Hinsch, K. D., Gausepohl, H., Frank, R., Schultz, G., and Böhme, E. (1990) *Eur. J. Biochem.* **190**, 273–278
11. Wedel, B., Humbert, P., Harteneck, C., Foerster, J., Malkewitz, J., Böhme, E., Schultz, G., and Koesling, D. (1994) *Proc. Natl. Acad. Sci. U.S.A.* **91**, 2592–2596
12. Zhao, Y., and Marletta, M. A. (1997) *Biochemistry* **36**, 15959–15964
13. Deinum, G., Stone, J. R., Babcock, G. T., and Marletta, M. A. (1996) *Biochemistry* **35**, 1540–1547
14. Makino, R., Matsuda, H., Obayashi, E., Shiro, Y., Iizuka, T., and Hori, H. (1999) *J. Biol. Chem.* **274**, 7714–7723
15. Ignarro, L. J., Wood, K. S., and Wolin, M. S. (1982) *Proc. Natl. Acad. Sci. U.S.A.* **79**, 2870–2873
16. Gerzer, R., Hofmann, F., and Schultz, G. (1981) *Eur. J. Biochem.* **116**, 479–486
17. Makino, R., Obayashi, E., Homma, N., Shiro, Y., and Hori, H. (2003) *J. Biol. Chem.* **278**, 11130–11137
18. Nioche, P., Berka, V., Vipond, J., Minton, N., Tsai, A. L., and Raman, C. S. (2004) *Science* **306**, 1550–1553
19. Pellicena, P., Karow, D. S., Boon, E. M., Marletta, M. A., and Kuriyan, J. (2004) *Proc. Natl. Acad. Sci.* **101**, 12854–12859
20. Boon, E. M., Huang, S. H., and Marletta, M. A. (2005) *Nat. Chem. Biol.* **1**, 53–59
21. Hu, X., Murata, L. B., Weichsel, A., Brailey, J. L., Roberts, S. A., Nighorn, A., and Montfort, W. R. (2008) *J. Biol. Chem.* **283**, 20968–20977
22. Martin, E., Berka, V., Bogatenkova, E., Murad, F., and Tsai, A. L. (2006) *J. Biol. Chem.* **281**, 27836–27845
23. Derbyshire, E. R., Deng, S., and Marletta, M. A. (2010) *J. Biol. Chem.* **285**, 17471–17478
24. Yazawa, S., Tsuchiya, H., Hori, H., and Makino, R. (2006) *J. Biol. Chem.* **281**, 21763–21770
25. Hagihara, B., and Iizuka, T. (1971) *J. Biochem.* **69**, 355–362
26. Binsted, N., Strange, R. W., and Hasnain, S. S. (1992) *Biochemistry* **31**, 12117–12125
27. Obayashi, E., Tsukamoto, K., Adachi, S., Takahashi, S., Nomura, M., Iizuka, T., Shoun, H., and Shiro, Y. (1997) *J. Am. Chem. Soc.* **119**, 7807–7816
28. Miyatake, H., Mukai, M., Adachi, S., Nakamura, H., Tamura, K., Iizuka, T., Shiro, Y., Strange, R. W., and Hasnain, S. S. (1999) *J. Biol. Chem.* **274**, 23176–23184
29. Tsujimura, S., Kuriyama, A., Fujieda, N., Kano, K., and Ikeda, T. (2005) *Anal. Biochem.* **337**, 325–331
30. Makino, R., and Yamazaki, I. (1974) *Arch. Biochem. Biophys.* **165**, 485–493
31. Seybert, D. W., Moffat, K., Gibson, Q. H., and Chang, C. K. (1977) *J. Biol. Chem.* **252**, 4225–4231
32. Yonetani, T., Yamamoto, H., and Woodrow, G. V., 3rd (1974) *J. Biol. Chem.* **249**, 682–690
33. Ikeda-Saito, M., Iizuka, T., Yamamoto, H., Kayne, F. J., and Yonetani, T. (1977) *J. Biol. Chem.* **252**, 4882–4887
34. Hori, H., Ikeda-Saito, M., and Yonetani, T. (1982) *J. Biol. Chem.* **257**, 3636–3642
35. Eisenberger, P., Shulman, R. G., Kincaid, B. M., Brown, G. S., and Ogawa, S. (1978) *Nature* **274**, 30–34
36. Stone, J. R., Sands, R. H., Dunham, W. R., and Marletta, M. A. (1995) *Biochem. Biophys. Res. Commun.* **207**, 572–577
37. Li, T., Quillin, M. L., Phillips, G. N., Jr., and Olson, J. S. (1994) *Biochemistry*

## Oxy Form of Guanylate Cyclase

- 33, 1433–1446
38. Yang, F., and Phillips, G. N., Jr. (1996) *J. Mol. Biol.* **256**, 762–774
39. Rich, A. M., Armstrong, R. S., Ellis, P. L., and Lay, P. A. (1998) *J. Am. Chem. Soc.* **120**, 10827–10836
40. Huang, S. H., Rio, D. C., and Marletta, M. A. (2007) *Biochemistry* **46**, 15115–15122
41. Mims, M. P., Porras, A. G., Olson, J. S., Noble, R. W., and Peterson, J. A. (1983) *J. Biol. Chem.* **258**, 14219–14232
42. Derbyshire, E. R., and Marletta, M. A. (2007) *J. Biol. Chem.* **282**, 35741–35748
43. Evans, J. P., Kandel, S., and Ortiz de Montellano, P. R. (2009) *Biochemistry* **48**, 8920–8928
44. Stetzkowski, F., Cassoly, R., and Banerjee, R. (1979) *J. Biol. Chem.* **254**, 11351–11356
45. Derbyshire, E. R., Tran, R., Mathies, R. A., and Marletta, M. A. (2005) *Biochemistry* **44**, 16257–16265
46. Marti, M. A., Crespo, A., Capece, L., Boechi, L., Bikiel, D. E., Scherlis, D. A., and Estrin, D. A. (2006) *J. Inorg. Biochem.* **100**, 761–770
47. Collman, J. P., Brauman, J. I., Iverson, B. L., Seeler, J. L., Morris, R. M., and Gibson, Q. M. (1983) *J. Am. Chem. Soc.* **105**, 3052–3064
48. Oberting, W. A., Kean, R. T., Wever, R., and Babcock, G. T. (1990) *Inorg. Chem.* **29**, 2633–2645
49. Traylor, T. G., Duprat, A. F., and Sharma, V. S. (1993) *J. Am. Chem. Soc.* **115**, 810–811
50. Gullotti, M., Santagostini, L., Monzani, E., and Casella, L. (2007) *Inorg. Chem.* **46**, 8971–8975
51. Falk, J. E. (1964) *Porphyrins and Metalloporphyrins*, pp. 67–71, Elsevier Publishing Co., Amsterdam
52. Faulkner, K. M., Bonaventura, C., and Crumbliss, A. L. (1995) *J. Biol. Chem.* **270**, 13604–13612

## Dual Regulation of the Transcriptional Activity of Nrf1 by $\beta$ -TrCP- and Hrd1-Dependent Degradation Mechanisms<sup>∇</sup>

Yoshiki Tsuchiya,<sup>1</sup>† Tomoko Morita,<sup>1</sup>† Mehee Kim,<sup>1</sup> Shun-ichiro Iemura,<sup>2</sup> Tohru Natsume,<sup>2</sup> Masayuki Yamamoto,<sup>3</sup> and Akira Kobayashi<sup>1\*</sup>

Laboratory for Genetic Cord, Graduate School of Life and Medical Sciences, Doshisha University, 1-3 Tatara Miyakodani, Kyotanabe 610-0394,<sup>1</sup> National Institutes of Advanced Industrial Science and Technology, Biological Information Research Center, Kohtoh-ku, Tokyo 135-0064,<sup>2</sup> and Department of Medical Biochemistry and ERATO-JST, Tohoku University Graduate School of Medicine, Aoba-ku, Sendai 980-8575,<sup>3</sup> Japan

Received 22 May 2011/Returned for modification 19 June 2011/Accepted 3 September 2011

**A growing body of evidence suggests that Nrf1 is an inducible transcription factor that maintains cellular homeostasis. Under physiological conditions, Nrf1 is targeted to the endoplasmic reticulum (ER), implying that it translocates into the nucleus in response to an activating signal. However, the molecular mechanisms by which the function of Nrf1 is modulated remain poorly understood. Here, we report that two distinct degradation mechanisms regulate Nrf1 activity and the expression of its target genes. In the nucleus,  $\beta$ -TrCP, an adaptor for the SCF (Skp1-Cul1-F-box protein) ubiquitin ligase, promotes the degradation of Nrf1 by catalyzing its polyubiquitination. This activity requires a DSGLS motif on Nrf1, which is similar to the canonical  $\beta$ -TrCP recognition motif. The short interfering RNA (siRNA)-mediated silencing of  $\beta$ -TrCP markedly augments the expression of Nrf1 target genes, such as the proteasome subunit PSMC4, indicating that  $\beta$ -TrCP represses Nrf1 activation. Meanwhile, in the cytoplasm, Nrf1 is degraded and suppressed by the ER-associated degradation (ERAD) ubiquitin ligase Hrd1 and valosin-containing protein (VCP) under normal conditions. We identified a cytoplasmic degradation motif on Nrf1 between the NHB1 and NHB2 domains that exhibited species conservation. Thus, these results clearly suggest that both  $\beta$ -TrCP- and Hrd1-dependent degradation mechanisms regulate the transcriptional activity of Nrf1 to maintain cellular homeostasis.**

The transcription factor Nrf1 (NF-E2-related factor 1 or NFE2L1) belongs to the cap'n-collar-type basic leucine zipper (CNC-bZip) protein family. Nrf1 activates gene expression through either the antioxidant response element (ARE) or the Maf recognition element (MARE) by heterodimerizing with small Maf proteins (14, 32). The physiological roles of Nrf1 remain unclear, but gene-targeting experiments have helped to elucidate the function of Nrf1. Nrf1-deficient mice display an embryonic lethal phenotype due to anemia (3). The conditional gene targeting of Nrf1 in hepatocytes, osteoblasts, and neural cells causes steatosis, diminished bone formation, and neurodegeneration, respectively (10, 13, 23, 36, 37). These *in vivo* observations clearly indicate that Nrf1 is indispensable to the maintenance of cellular homeostasis. Recent studies have demonstrated that Nrf1 regulates expression of a set of proteasome subunit genes to maintain proteasome homeostasis (27, 31). Extensive biochemical studies have also elucidated the molecular regulation of Nrf1. Under physiological conditions, Nrf1 is anchored to the endoplasmic reticulum (ER) by its N-terminal NHB1 domain (34, 40, 42). This finding suggests that Nrf1-mediated gene expression requires activating stresses or signals that lead to the liberation of Nrf1 from the ER and,

thereby, the nuclear translocation of Nrf1. Supporting this idea, a number of studies have reported that several drugs, including tunicamycin, *tert*-butyl hydroquinone (tBHQ), ascorbic acid, and arsenite, promote the nuclear entry of Nrf1 (34, 36, 41, 44) although the precise mechanisms of their activities have not been fully elucidated.

The ubiquitin-proteasome system serves a central regulatory function by modulating the abundance of proteins in many biological processes, such as cell cycle progression, signal transduction, and transcription. The polyubiquitin chain, an important degradation signal recognized by the proteasome, is conjugated to substrate proteins by sequential reactions catalyzed by three types of enzymes (7, 28): the ubiquitin-activating enzymes (E1), the ubiquitin-conjugating enzymes (E2), and the ubiquitin ligases (E3). The E3 ubiquitin ligases exhibit two distinct functions; one function is to target substrate proteins, and the other function is to catalyze the formation of isopeptide bonds between the substrate protein and ubiquitin. Based on structural similarities, the E3 ubiquitin ligases are classified into three groups: the RING-finger proteins, the HECT domain proteins, and the U-box domain proteins. Among the RING-finger proteins, the SCF (Skp1-Cul1-F-box protein) ubiquitin ligases have been thoroughly characterized (5, 20). The SCF complex comprises the F-box protein, Skp1, and Cul1. The F-box protein functions as an adaptor that determines target specificity and recruits the target protein into the Cul1 scaffold along with Skp1. Sixty-nine F-box proteins, including  $\beta$ -TrCP (the  $\beta$ -transducin repeat-containing protein), have been identified in humans.  $\beta$ -TrCP regulates various cellular processes by mediating the degradation of target proteins,

\* Corresponding author. Mailing address: Laboratory for Genetic Cord, Graduate School of Life and Medical Sciences, Doshisha University, 1-3, Tatara Miyakodani, Kyotanabe 610-0394, Japan. Phone: 81 774 65 6273. Fax: 81 774 65 6274. E-mail: akobayas@mail.doshisha.ac.jp.

† Y.T. and T.M. contributed equally to this paper.

∇ Published ahead of print on 12 September 2011.

such as I $\kappa$ B,  $\beta$ -catenin, and Cdc25, which are intimately related to tumorigenesis. Mammals express two distinct paralogues of this protein,  $\beta$ -TrCP1 and  $\beta$ -TrCP2, which exhibit similar biochemical properties (thus, the paralogues will here be referred to as  $\beta$ -TrCP).  $\beta$ -TrCP recognizes a consensus DpSGX<sub>n</sub>pS motif ( $n \geq 1$ ; pS represents the phosphorylated serine residue) or variants of this motif in its substrates via its WD40 repeat domain. In the case of the former canonical motif, phosphorylation of its conserved serine residues is indispensable for the recognition of specific substrates by  $\beta$ -TrCP. Numerous reports have documented that the phosphorylation of the substrates of  $\beta$ -TrCP is catalyzed by specific kinases, such as glycogen synthase kinase 3 $\beta$  (GSK-3 $\beta$ ), polo-like kinase, and CK1.

The endoplasmic reticulum-associated degradation (ERAD) is a quality control system for misfolded or improperly assembled membrane proteins and secreted proteins in the ER (1, 8). Such aberrant proteins are polyubiquitinated by ubiquitin ligases, comprising multiple protein subunits, in the ER membrane. These components are conserved in all eukaryotic organisms, strongly suggesting the importance of this process to cellular homeostasis. One of the ERAD ubiquitin ligases, Hrd1 (also known as synoviolin), forms a complex with SEL1L and predominantly mediates the degradation of soluble, ER-luminal substrates and integral membrane proteins. After being polyubiquitinated by the Hrd1-SEL1L complex, the substrates are recognized by a complex containing the AAA-ATPase p97/valosin-containing protein (VCP) and are transported to the proteasome. Intriguingly, Hrd1 has been reported to control the turnover of p53 in the cytoplasm (38). This finding indicates that Hrd1 contributes to the degradation of cytoplasmic factors as well as ERAD.

To understand the physiological roles of Nrf1, we first attempted to elucidate the regulatory mechanism of Nrf1. In this regard, the growing body of evidence regarding the molecular basis of the stress response mediated by the Nrf1-related factor Nrf2 provided considerable insight. Nrf2 is one of the major regulatory factors to induce the expression of oxidative stress response genes, such as heme oxygenase-1 (*Ho-1*) and *Nqo1*, in response to oxidative stress (32). Under physiological conditions, Nrf2 is sequestered in the cytoplasm by the oxidative stress sensor Keap1. Moreover, Keap1 possesses an additional function as an adaptor protein for the Cul3-based ubiquitin ligase and, thereby, mediates the polyubiquitin conjugation and proteasomal degradation of Nrf2. Importantly, the nature of the activation mechanism of Nrf2 in response to oxidative stress is the inhibition of the Keap1-mediated ubiquitination of Nrf2, which results in the nuclear entry of stabilized Nrf2 (12). Based on these findings, we hypothesized that the function of Nrf1 is also regulated in a ubiquitin-proteasome-dependent fashion and investigated this hypothesis in the current study. Here, we report that the transcriptional activity of Nrf1 is modulated by two distinct degradation pathways in the nucleus and the cytoplasm. The nuclear degradation of Nrf1 is mediated by the ubiquitin ligase adaptor  $\beta$ -TrCP, which results in the repression of the transcriptional activity of Nrf1. The cytoplasmic degradation of Nrf1 is dependent on Hrd1 and VCP. Collectively, these results suggest that the regulation of two proteolysis pathways induces the transcriptional activation by Nrf1 to maintain cellular homeostasis.

## MATERIALS AND METHODS

**Antibodies.** The antibodies utilized in this study included anti-Flag (M2; Sigma), anti-hemagglutinin ([HA] Y-11; Santa Cruz), anti-Myc (A-14; Santa Cruz), anti-green fluorescent protein ([GFP] B-2; Santa Cruz), anti-Nrf1 (H-285; Santa Cruz), anti-Nrf2 (H-300; Santa Cruz), anti- $\beta$ -catenin (BD Biosciences), anti- $\alpha$ -tubulin (Sigma), and anti-lamin B1 (Zymed). The rat monoclonal anti-Keap1 antibody was described previously (35). Rat monoclonal antibodies directed against mouse Nrf1 were raised by immunizing rats with a purified recombinant Nrf1 protein (residues 211 to 460), tagged with six histidine residues, that was expressed in *Escherichia coli*. After hybridoma cells expressing antibodies were selected, one positive clone for Nrf1 (clone 17) was injected into the abdominal cavity of a mouse to produce ascites, and the resultant antibody was purified from ascites using a protein G column (Pierce).

**Plasmid construction.** All expression plasmids of Flag-tagged wild-type (WT) Nrf1 and deletion mutants were generated by subcloning the cDNA fragments encoding various Nrf1 mutants that were amplified by PCR into the Asp718 and XbaI sites of pcDNA3 (Invitrogen). HA-tagged wild-type  $\beta$ -TrCP2 and  $\Delta$ F-box mutant expression vectors were kindly provided by Keiko Nakayama (Tohoku University). The HA- $\beta$ -TrCP2  $\Delta$ WD40 expression vector was constructed through the PCR-based amplification method. The Myc-tagged  $\beta$ -TrCP2 expression vector was constructed by subcloning  $\beta$ -TrCP2 into the pcDNA3-Myc vector. The Flag-tagged Nrf2 was generated as described previously (9). The HA-tagged ubiquitin vector was kindly provided by Dirk Bohmann (33). The 3 $\times$ PSMA4-ARE-Luc vector was kindly provided by Raymond J. Deshaies (27). All constructions were verified by DNA sequencing. Detailed information regarding all expression vectors is available upon request.

**Cell culture and transfection.** COS7 cells and HeLa cells were cultured in Dulbecco's modified Eagle's medium (DMEM) (Wako) supplemented with 10% fetal calf serum (FCS) (Invitrogen), 4,500 mg/liter glucose, 40  $\mu$ g/ml streptomycin, and 40 units/ml penicillin. Mouse embryonic fibroblasts (MEFs) were cultured in Iscove's modified Dulbecco's medium (IMDM) (Wako) supplemented with 10% FCS, 2 mM glutamine (Invitrogen), 40  $\mu$ g/ml streptomycin, and 40 units/ml penicillin. The transfection of plasmid DNA and short interfering RNA (siRNA) was achieved by Lipofectamine Plus and Lipofectamine 2000 (Invitrogen), respectively.

**Immunoprecipitation and immunoblot analysis.** Expression plasmids for wild-type or deletion mutants of HA- $\beta$ -TrCP2 were transfected into COS7 cells along with wild-type or deletion mutants of Nrf1 with three copies of the Flag tag (3 $\times$ Flag-Nrf1). At 24 h after transfection, cells were treated with the protease inhibitor MG132 (Peptide Institute) at a concentration of 10  $\mu$ M for 8 h and subjected to preparation of whole-cell extracts with lysis buffer (50 mM Tris-HCl [pH 8.0], 10% glycerol, 100 mM NaF, 50 mM NaCl, 2 mM EDTA, 2 mM sodium orthovanadate, 10 mM sodium pyrophosphate, 10 mM  $\beta$ -glycerophosphate, 0.1% NP-40, and 1 $\times$  protease inhibitor cocktail [Roche]). The whole-cell extracts were subjected to immunoprecipitation with anti-Flag M2 affinity gels (Sigma) at 4°C for 2 h. After the affinity gels were washed with a wash buffer (50 mM Tris-HCl [pH 7.4], 150 mM NaCl and 0.1% NP-40) three times, immunocomplexes were eluted by boiling in an SDS sample buffer (50 mM Tris-HCl [pH 6.8], 10% glycerol and 1% SDS) and subjected to immunoblot analysis using the antibodies indicated on the figures. The blots were treated with a horseradish peroxidase-conjugated secondary antibody (Invitrogen) and were developed with enhanced chemiluminescence (ECL; GE Healthcare).

**Cycloheximide chase experiment.** Expression vectors encoding wild-type 3 $\times$ Flag-Nrf1 or deletion mutants were transfected into COS7 cells along with a GFP expression vector, which served as an internal control. At 24 h after transfection, the cells were treated with 20  $\mu$ g/ml cycloheximide, and at the indicated time points, the whole-cell extracts were prepared and subjected to immunoblot analysis with the antibodies indicated on the figures. For the analysis of endogenous proteins, the cells were pretreated with 10  $\mu$ M MG132 for 6 h, washed two times with phosphate-buffered saline (PBS), and treated with 20  $\mu$ g/ml cycloheximide.

**Subcellular fractionation of MEFs.** MEFs derived from wild-type and Nrf1 knockout mice were grown in six-well plates and left untreated or treated with 10  $\mu$ M MG132 for 8 h. The method of the preparation of cytoplasmic and nuclear extracts was described previously (12). Briefly, the cells were swollen in buffer A (20 mM HEPES-KOH [pH 8.0], 10 mM KCl, 1.5 mM MgCl<sub>2</sub>, 0.1 mM EDTA, 1 mM dithiothreitol [DTT], 1 $\times$  protease inhibitor cocktail [Roche], and 10  $\mu$ M MG132), followed by lysis with the addition of NP-40 (at a final concentration of 2.5%). After centrifugation, the supernatants and precipitates were collected. The supernatants were further subjected to centrifugation at 20,000  $\times$  g for 10 min, and subsequent supernatants were employed as cytoplasmic extracts in the present study. On the other hand, the precipitates were subjected to two washes

with buffer A, lysis with the SDS sample buffer, and mild sonication to shear genomic DNA. After centrifugation, the supernatants were collected as nuclear extracts. The quantities of proteins in these extracts were determined with a bicinchoninic acid (BCA) kit (Thermo).

**Immunocytochemical staining.** COS7 cells transiently expressing wild-type 3×Flag-tagged Nrf1 or a deletion mutant or HA-β-TrCP2 were fixed with formaldehyde for 10 min, washed twice with PBS, and permeabilized with 0.5% Triton X-100 in PBS for 5 min. The cells were washed with PBS twice and treated with anti-Flag or anti-HA antibodies for 1 h at room temperature. After cells were washed three times with PBS, they were incubated with Alexa 488- or Alexa 546-conjugated secondary antibodies for 30 min at room temperature, and the nuclei were stained with 4',6'-diamidino-2-phenylindole (DAPI). After samples were washed with PBS, a drop of fluorescent mounting medium (Dako) was placed on the glass slides. Fluorescence images were captured by an Olympus IX71 microscope.

**siRNA knockdown experiment.** HeLa cells split into 12-well plates were cultured for 24 h in medium without antibiotics. The cells were transfected twice with 40 nM siRNA (at 24 and 48 h after plating) using Lipofectamine 2000 (Invitrogen). At 24 h after the last transfection, the cells were utilized for each experiment. For the cotransfection of siRNA and plasmid DNA, 40 nM siRNA was transfected into the cells along with plasmid DNA using Lipofectamine 2000 (Invitrogen). A GFP expression vector was also transfected into the cells as an internal control. At 24 h after transfection, the culture medium was replaced with fresh medium without antibiotics, and the cells were subsequently cultured for 24 h. The cells were lysed with an SDS sample buffer, and the resultant whole-cell extracts were subjected to immunoblot analysis with the antibodies indicated on the figures. The sequences of the sense strand of the siRNA duplexes employed in the present study were as follows: control siRNA, 5'-UUCUCCGAAACGUGUCACGUdTdT-3'; Nrf1, 5'-GGGAUUCGGUGAAGAUUUgTdT-3'; β-TrCP1(1), 5'-CAAUCUACACCGAAUCCcdTdT-3'; β-TrCP1(2), 5'-UUCUCACAGGCCAUACAGGdTdT-3'; β-TrCP2, 5'-GAGGCCAUACAGAAGGAAAcdTdT-3'; β-TrCP1/2, 5'-GUGGAAUUUGUGAACAUCdTdT-3'; Keap1, 5'-GGCCUUUGGCAUCAUGACdTdT-3'; VCP, 5'-GUAGGGUAUGAUGACAUGdTdT-3'; gp78, 5'-CAUGCAGAAUGUCUCUUAAdTdT-3'; TEB4, 5'-UUAAGAGUGUGUCGCCUAAAdTdT-3'. For the knockdown of Hrd1, siGENOME SMART pools of four oligonucleotide duplexes targeted against Hrd1 (Dharmacon) were used.

**RNA extraction and real-time quantitative PCR.** Total RNA was extracted from cells with an RNeasy Mini kit (Qiagen) and subjected to cDNA synthesis with random hexamer primers. Real-time quantitative PCR was performed with FastStart Universal SYBR (Roche) master mix and an ABI Prism 7900 (Applied Biosystems). The PCR primers employed in the present study were as follows: Nrf1, 5'-TGGAACAGCAGTGGCAAGATCTCA-3' and 5'-GGCAGTGTACAAGATTCACITGC-3'; β-TrCP1, 5'-TGCCGAAGTGAAACAAGC-3' and 5'-CCTGTGAGAATTTCGCTTG-3'; β-TrCP2, 5'-TCAGTGGCCTACGAGAT A-3' and 5'-ACAGCTCATCACTACTGCA-3'; glyceraldehyde-3-phosphate dehydrogenase (GAPDH), 5'-CCAGAACATCATCCCTGCCTCTACT-3' and 5'-GGTTTTTCTAGACGGCAGGTCAG-3'; 18S rRNA, 5'-CGCCGCTAGAGGTGAAATTC-3' and 5'-CGAACCTCCGACTTTCGTTCT-3'; Psmc4, 5'-GGAAGACCATGTTGGCAAAG-3' and 5'-AAGATGATGGCAGGTGCATT-3'; Psmc2, 5'-GCCCGATTACAGAGTGC-3' and 5'-TGGACGAACACCACCTGA-3'; Psmc4, 5'-CATTTGGCTGGGATAAGCA-3' and 5'-ATGCATGTGGCCTTCCAT-3'; VCP, 5'-TACCAACCGGCCTGACAT-3' and 5'-TGGCAACA CGGGACTTCT-3'; Hrd1, 5'-TGCAACCACATTTCCATACCA-3' and 5'-GCGATGCACGAAGGACATC-3'; gp78, 5'-GGTGCAGCGTAAGGACGA A-3' and 5'-GCATCATCTTCAGAACTTTTGTTC-3'; TEB4, 5'-TTGTCTTCCAAGTCCGCCAG-3' and 5'-GACTGTGGAGGTGGTGGAGATG-3'.

**The ubiquitination assay.** HeLa cells were transfected with expression plasmids encoding 3×Flag-Nrf1 P3 (Nrf1 with a deletion of residues 1 to 242) and HA-tagged ubiquitin along with plasmids expressing wild-type Myc-tagged β-TrCP2 or a ΔF-box β-TrCP2 mutant. At 24 h after transfection, the cells were treated with 10 μM MG132 for 8 h and were lysed with lysis buffer (10 mM Tris-HCl [pH 7.5], 150 mM NaCl, 1% SDS, 1× protease inhibitor cocktail [Roche], 10 μM MG132, and 10 mM *N*-ethylmaleimide [NEM]) to prepare the whole-cell extracts. The cell extracts were immediately boiled and diluted with dilution buffer (10 mM Tris-HCl [pH 7.5], 150 mM NaCl, 1% Triton X-100, 1× protease inhibitor cocktail, 10 μM MG132, and 10 mM NEM). After centrifugation at 18,000 × *g* for 15 min, the supernatants were incubated with anti-Flag antibody and protein G Sepharose beads (GE Healthcare) at 4°C for 2 h. The immunocomplexes were washed with dilution buffer twice and were eluted by boiling in an SDS sample buffer. Ubiquitinated Nrf1 was visualized by immunoblot analysis using anti-HA antibody.

**Luciferase assay.** The day before transfection, COS7 cells were split into 24-well plates and cultured for 24 h. The cells were transfected with plasmids encoding 3×Flag-Nrf1 P3 or the P3-SA mutant (with alanine substitutions at two serine residues of the motif Ser448/451) along with luciferase reporter plasmids encoding the NQO1 promoter (9) or three tandem copies of the ARE of PSMA4 (27), and cells were transfected with pRL-TK (Promega) as an internal control. At 24 h after transfection, luciferase activities were measured with the PicaGene luciferase assay system (Toyo Ink) and a Berthold Lumat LB9507 luminometer.

**Statistical analysis.** Data comparisons were conducted with a two-tailed Student's *t* test for repeated measurements.

## RESULTS

**The transcription factor Nrf1 is degraded in both the cytoplasm and the nucleus.** To evaluate our hypothesis that the biological function of Nrf1 is regulated in a proteasome-dependent manner, we first examined whether the proteasome inhibitor MG132 stabilizes the endogenous Nrf1 protein. We treated wild-type MEFs with MG132 for 8 h and prepared cytoplasmic and nuclear extracts from the cells. The expression level of Nrf1 was determined by immunoblot analysis with anti-Nrf1 antibody. The result indicates that MG132 treatment significantly enhanced multiple immunoreactive bands at 110 kDa (Fig. 1A, lanes 1 to 4). In contrast, MG132 treatment of Nrf1 knockout mouse-derived MEFs did not cause an increase in the immunoreactive bands (Fig. 1A, lanes 5 to 8), suggesting that the immunoreactive bands were derived from the endogenous Nrf1. Thus, we conclude that the turnover of Nrf1 is strongly dependent on proteasome activity.

This result also demonstrates that the Nrf1 protein accumulated predominantly in the nucleus upon treatment with MG132. As it has been reported that Nrf1 is localized to the ER membrane under normal conditions, we assumed that Nrf1 is constitutively degraded in the cytoplasm and that, after MG132 treatment, Nrf1 is stabilized and translocates into the nucleus. To test this hypothesis, we attempted to identify the cellular compartment where Nrf1 degradation occurs. Overexpressed wild-type (WT) full-length Nrf1 was localized to both the cytoplasm and the nucleus (Fig. 1B and C, WT). Thus, we generated Nrf1 mutants that predominantly localized to either the cytoplasm or the nucleus. As prior studies have reported that Nrf1 possesses an ER retention motif in the NHB1 domain and a nuclear localization signal (NLS) in the basic region of the bZip domain, we constructed Nrf1 mutants that lacked the NHB1 domain (P1) or the bZip domain (ΔbZip) (Fig. 1B). The subcellular localization of these Nrf1 mutants expressed in COS7 cells was determined by immunocytochemical staining with anti-Flag antibody. The result clearly indicates that the P1 mutant and the ΔbZip mutant predominantly localized to the nucleus and the cytoplasm, respectively (Fig. 1C). Utilizing these Nrf1 mutants, we investigated whether these mutant proteins undergo proteasome-mediated degradation. MG132 treatment stabilized wild-type Nrf1, implying that this assay closely mimics the degradation mechanism of endogenous Nrf1. Interestingly, not only the ΔbZip mutant but also the P1 mutant were significantly stabilized by MG132 treatment (Fig. 1D). This result clearly indicates that both mutant proteins are effectively degraded in a proteasome-dependent manner and strongly suggests that Nrf1 is degraded in both the cytoplasm and the nucleus.

**β-TrCP mediates the nuclear degradation of Nrf1.** To decipher the molecular basis underlying the cytoplasmic and nu-



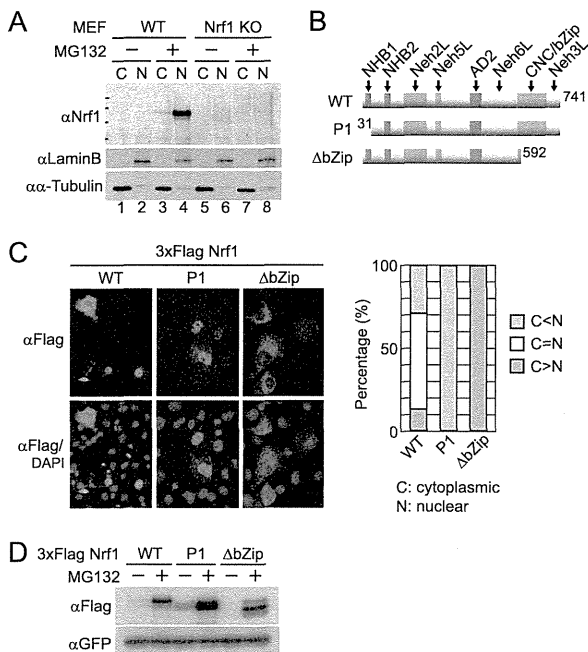


**FIG. 1.** The proteasomal degradation of the transcription factor Nrf1 in the cytoplasm and the nucleus. (A) MG132 stabilized the endogenous Nrf1 in MEFs. MEFs derived from wild-type (WT) and Nrf1 knockout (Nrf1 KO) mice were treated with MG132 (10  $\mu$ M) for 8 h. Cytoplasmic (C) and nuclear (N) extracts from the cells were subjected to immunoblot analysis with rat monoclonal anti-Nrf1 antibody. Lamin B1 and  $\alpha$ -tubulin were utilized as nuclear and cytoplasmic markers, respectively. (B) Schematic structures of the wild type and of the P1 and  $\Delta$ bZip deletion mutants of Nrf1. The domain nomenclature was defined previously (40). The numbers denote the positions of the amino acid residues in the complete sequence of Nrf1. (C) The P1 and  $\Delta$ bZip Nrf1 mutants predominantly localized in the nucleus and the cytoplasm, respectively, of COS7 cells. Nrf1 wild-type and mutants were stained with anti-Flag antibody, and the nuclei were stained with DAPI. A bar graph depicts the results of a quantitative analysis of the subcellular localization of the Nrf1 wild-type and mutants. More than 100 transfected cells were observed for the expression of each plasmid and classified into three different categories: C < N, nucleus-dominant staining; C = N, roughly equal distribution between the cytoplasmic and nuclear compartments; C > N, cytoplasm-dominant staining. (D) Both the P1 and  $\Delta$ bZip Nrf1 mutants were degraded by the proteasome in COS7 cells. Cells were treated with MG132 (10  $\mu$ M) for 8 h, and the expression levels of Nrf1 wild-type and deletion mutants were analyzed by immunoblot analysis with anti-Flag antibody. GFP was coexpressed as an internal control.  $\alpha$ , anti.

clear degradation of Nrf1, we attempted to identify the molecular component(s) that regulates Nrf1 proteolysis by using a proteomic approach (21). Whole-cell extracts from HEK293 cells expressing C-terminal Flag-tagged Nrf1 were subjected to immunoprecipitation with anti-Flag antibody to isolate Nrf1 complexes. Subsequent liquid chromatography-tandem mass spectrometry (LC-MS/MS) analyses identified a variety of proteins, including transcriptional cofactors, kinases, and protein modification enzymes, as Nrf1-associated molecules (data not shown). Importantly, the ubiquitination-related factors  $\beta$ -TrCP2, Skp1, and Keap1 were identified as Nrf1-binding factors. The  $\beta$ -TrCP2-Skp1 heterodimer and Keap1

are substrate-specific adaptors for the Cul1- and Cul3-based ubiquitin ligase complexes, respectively. Accordingly, we performed siRNA-mediated RNA interference experiments to examine whether  $\beta$ -TrCP2 and Keap1 are involved in the mechanism of Nrf1 degradation. Taking into consideration the functional redundancy between  $\beta$ -TrCP2 and its analogue  $\beta$ -TrCP1, we first examined the effect of siRNA against  $\beta$ -TrCP1,  $\beta$ -TrCP2, or both proteins ( $\beta$ -TrCP1/2) on the stability of Flag-tagged Nrf1 expressed in HeLa cells. Whole-cell extracts were prepared from the cells and were subjected to immunoblot analysis with anti-Flag antibody to examine the expression level of Nrf1. As a result, the knockdown of both  $\beta$ -TrCP1 and  $\beta$ -TrCP2 significantly stabilized the Nrf1 protein, whereas the knockdown of  $\beta$ -TrCP2 alone demonstrated a much smaller effect on Nrf1 stability (Fig. 2A). The silencing efficiency of  $\beta$ -TrCP1 and  $\beta$ -TrCP2 was confirmed by a real-time quantitative PCR analysis (Fig. 2B). Therefore, we employed siRNA specific to both  $\beta$ -TrCP1 and  $\beta$ -TrCP2 in all subsequent experiments. Next, we investigated the effect of  $\beta$ -TrCP siRNA on the stability of the Nrf1 mutants. Interestingly,  $\beta$ -TrCP siRNA significantly stabilized the P1 mutant but not the  $\Delta$ bZip mutant while MG132 treatment stabilized both mutants (Fig. 2C). Real-time quantitative PCR analysis demonstrated that the  $\beta$ -TrCP siRNA significantly reduced both  $\beta$ -TrCP1 and  $\beta$ -TrCP2 mRNAs but not Nrf1 mRNA (Fig. 2D). These data indicate that Nrf1 degradation is regulated by both  $\beta$ -TrCP-dependent and -independent mechanisms. Given that the P1 and  $\Delta$ bZip mutants exhibit distinct intracellular localizations (Fig. 1C), it is likely that  $\beta$ -TrCP-dependent degradation of Nrf1 occurs predominantly in the nucleus. Meanwhile, Keap1 siRNA did not stabilize the wild-type Nrf1 or the P1 or  $\Delta$ bZip mutant (Fig. 2C and E, left panel) although it stabilized Nrf2 (Fig. 2E, right panel). These results indicate that Keap1 is not involved in the regulation of Nrf1 degradation.

To confirm further the  $\beta$ -TrCP-dependent degradation of Nrf1, we addressed the question of whether  $\beta$ -TrCP siRNA stabilizes the endogenous Nrf1 protein. Unexpectedly,  $\beta$ -TrCP siRNA alone did not stabilize Nrf1 in HeLa cells (data not shown), probably because the endogenous Nrf1 is predominantly localized to the ER membrane and is primarily degraded in the cytoplasm rather than in the nucleus. Because MG132 treatment causes the nuclear accumulation of Nrf1 in MEFs (Fig. 1A), we performed cycloheximide chase experiments using HeLa cells pretreated with MG132. As a result,  $\beta$ -TrCP siRNA significantly suppressed the degradation of the endogenous Nrf1 (Fig. 2F, 1/2) as well as that of  $\beta$ -catenin, a canonical  $\beta$ -TrCP substrate. Taken together, these findings indicate that  $\beta$ -TrCP regulates the nuclear degradation of Nrf1.

**Colocalization and physical interaction of Nrf1 and  $\beta$ -TrCP.** To understand the molecular basis of the  $\beta$ -TrCP-mediated degradation of Nrf1, we investigated the subcellular colocalization of Nrf1 and  $\beta$ -TrCP2 by immunostaining. The 3xFlag-tagged Nrf1 and HA-tagged  $\beta$ -TrCP2 expressed in COS7 cells were visualized with anti-Flag and anti-HA antibodies, respectively. We observed significant colocalization of Nrf1 and  $\beta$ -TrCP2 (Fig. 3A). Next, we assessed the physical interaction between Nrf1 and  $\beta$ -TrCP2 by immunoprecipitation analysis. Whole-cell extracts from COS7 cells expressing both factors were subjected to immunoprecipitation with anti-Flag anti-

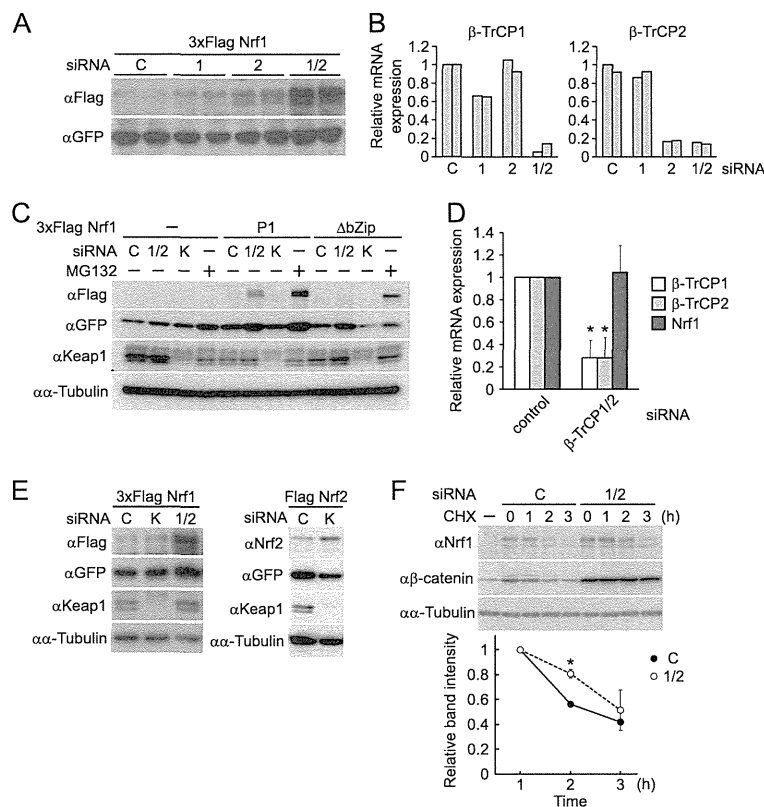


FIG. 2. The  $\beta$ -TrCP protein regulates the nuclear degradation of Nrf1. (A) HeLa cells were transfected with the 3 $\times$ Flag-Nrf1 and GFP expression vectors at 24 h after two rounds of transfection with control (C),  $\beta$ -TrCP1 (1),  $\beta$ -TrCP2 (2), or  $\beta$ -TrCP1/2 (1/2) siRNA. At 24 h after the last transfection, whole-cell extracts were prepared and subjected to immunoblot analysis. Duplicate samples are presented. (B) The knockdown efficiency of each siRNA for  $\beta$ -TrCP1 and  $\beta$ -TrCP2 was determined by real-time quantitative PCR analysis. Duplicate samples are presented. (C) HeLa cells were transfected with siRNA against  $\beta$ -TrCP1 and  $\beta$ -TrCP2 (1/2), Keap1 (K), or the control (C) along with 3 $\times$ Flag-tagged P1 and the  $\Delta$ bZip Nrf1 mutant. Cells were left untreated or treated with MG132 (10  $\mu$ M) for 8 h. Cell extracts were subjected to immunoblot analysis with the indicated antibodies. (D) Real-time quantitative PCR analysis revealed that siRNA directed against  $\beta$ -TrCP significantly reduced mRNA expression of both  $\beta$ -TrCP1 and  $\beta$ -TrCP2 but not Nrf1 in HeLa cells. The values were normalized with GAPDH and are presented as the means  $\pm$  standard deviations ( $n = 3$ ; \*,  $P < 0.001$ ). (E) Control (C), Keap1 (K), or  $\beta$ -TrCP1/2 (1/2) siRNA was transfected into HeLa cells in combination with the 3 $\times$ Flag-Nrf1 vector or the Flag Nrf2 vector. Whole-cell extracts were subjected to immunoblot analysis with the indicated antibodies. (F) The siRNA directed against  $\beta$ -TrCP stabilized the endogenous Nrf1.  $\beta$ -TrCP (1/2) or the control (C) siRNA was twice transfected into HeLa cells. At 48 h after the second transfection, the cells were pretreated with MG132 (10  $\mu$ M) for 6 h and treated with cycloheximide (CHX) (20  $\mu$ g/ml). Whole-cell extracts were prepared for immunoblot analysis with anti-Nrf1 (H-285) antibody. The  $\beta$ -catenin protein is a canonical  $\beta$ -TrCP substrate, and  $\alpha$ -tubulin is an internal control. The graph depicts the quantified band intensities of Nrf1. The values were normalized with  $\alpha$ -tubulin and are presented as the means  $\pm$  standard error ( $n = 3$ ; \*,  $P < 0.005$ ). The values at 1 h after cycloheximide treatment were set to 1.

body-conjugated beads. Immunoblot analysis with anti-HA antibody revealed that  $\beta$ -TrCP2 was coimmunoprecipitated with Nrf1 (Fig. 3B). These results demonstrate that  $\beta$ -TrCP interacts with Nrf1.

**Identification of the association interfaces between Nrf1 and  $\beta$ -TrCP.** We then defined the association interfaces between Nrf1 and  $\beta$ -TrCP with an immunoprecipitation assay. To this end, we generated a series of deletion mutants of  $\beta$ -TrCP2 and Nrf1 (Fig. 3C and E). The  $\beta$ -TrCP protein is composed of the F-box and WD40 repeat domains, and the latter is known as the substrate-binding domain. An immunoprecipitation assay demonstrated that deletion of the WD40 repeat domain, but not the F-box domain, from  $\beta$ -TrCP2 significantly compro-

mised its interaction with Nrf1 (Fig. 3D,  $\Delta$ WD), indicating that  $\beta$ -TrCP2 interacts with Nrf1 via the WD40 repeat domain.

Next, we analyzed the  $\beta$ -TrCP binding region within Nrf1. We coexpressed a series of 3 $\times$ Flag-tagged, N-terminal deletion mutants of Nrf1 with HA-tagged  $\beta$ -TrCP2 in COS7 cells. Nrf1 mutants were then immunoprecipitated with anti-Flag antibody, and the precipitates were analyzed by immunoblotting. The result clearly indicates that the P2 (Nrf1 with a deletion of residues 1 through 106) and P3 mutants associate with  $\beta$ -TrCP but that the P4 mutant (deletion of residues 1 through 463) did not (Fig. 3F, lanes 3 to 7), indicating that residues 243 to 463 of Nrf1 could be recognized by  $\beta$ -TrCP. On the other hand, the analysis using internal deletion mutants of

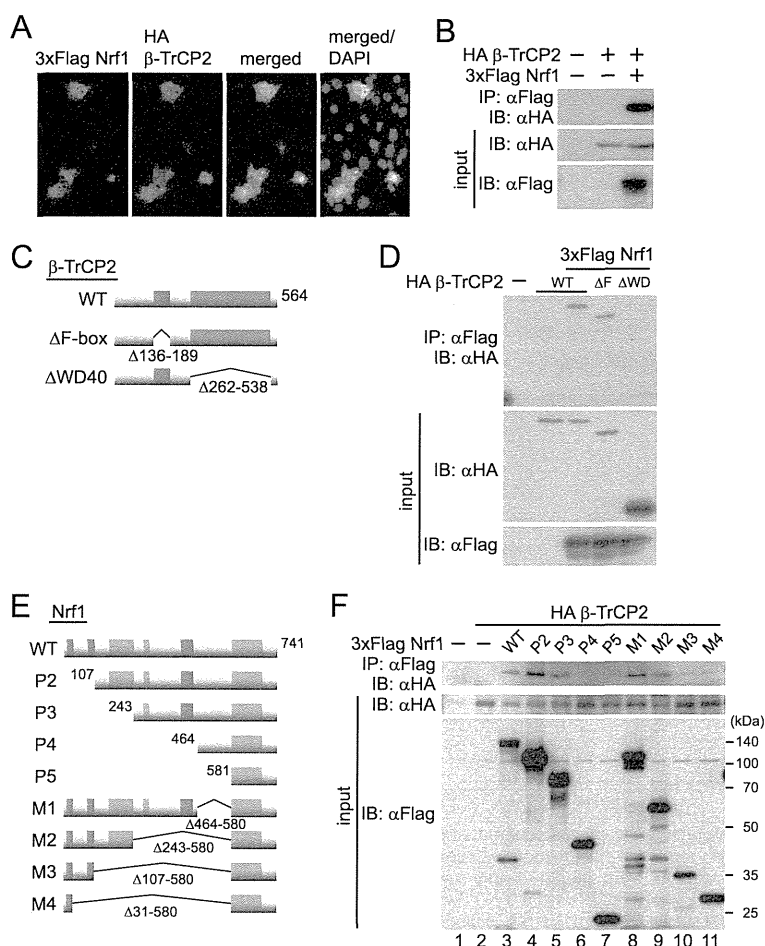


FIG. 3. Colocalization and physical interaction of Nrf1 with  $\beta$ -TrCP2. (A) Colocalization of wild-type Nrf1 with  $\beta$ -TrCP2 in COS7 cells. The 3 $\times$ Flag-Nrf1 and HA- $\beta$ -TrCP2 expressed in COS7 cells were immunostained with the indicated antibodies. (B) Physical interaction of Nrf1 with  $\beta$ -TrCP2. Whole-cell extracts of COS7 cells expressing 3 $\times$ Flag-Nrf1 and HA-tagged  $\beta$ -TrCP2 were subjected to immunoprecipitation (IP) with anti-Flag antibody, followed by immunoblot (IB) analysis with the indicated antibodies. (C) Schematic structures of  $\beta$ -TrCP2 deletion mutants.  $\beta$ -TrCP2 comprises the F-box and WD40 repeat domains. (D) The WD40 repeat domain of  $\beta$ -TrCP2 was required for its association with Nrf1. The 3 $\times$ Flag-Nrf1 and the HA- $\beta$ -TrCP2 wild type (WT) or  $\Delta$ F-box ( $\Delta$ F) or  $\Delta$ WD40 ( $\Delta$ WD) mutant were expressed into COS7 cells, and immunoprecipitation with anti-Flag antibody was performed, as described above. (E) Schematic structures of Nrf1 deletion mutants. (F) Identification of  $\beta$ -TrCP2-binding regions within Nrf1. Immunoprecipitation with anti-Flag antibody was performed, as described above. To ensure that the Nrf1 mutant proteins were expressed at similar levels, we transfected various amounts of plasmids, as follows: WT and M1, 1  $\mu$ g; P2, P3, and M2, 0.3  $\mu$ g; P4, P5, M3, and M4, 30 ng.

Nrf1 indicates that the M2 mutant, but not the M3 mutant, can interact with  $\beta$ -TrCP. Thus, residues 107 to 242 may represent another  $\beta$ -TrCP-binding interface (Fig. 3F, lanes 8 to 11). These results collectively indicate that at least two regions within Nrf1 can interact with  $\beta$ -TrCP.

**An internal region (residues 243 to 463) of Nrf1 is required for its  $\beta$ -TrCP-dependent nuclear degradation.** To further identify the amino acid region responsible for the  $\beta$ -TrCP-dependent degradation of Nrf1, we examined the effect of  $\beta$ -TrCP knockdown on the stability of Nrf1 mutants. In N-terminal deletion analysis,  $\beta$ -TrCP siRNA stabilized the P2 and P3 Nrf1 mutants, as well as wild-type Nrf1 (Fig. 4A, lanes 3 to 8). However,  $\beta$ -TrCP siRNA did not change the expression level of the P4 mutant (Fig. 4A, lanes 9 and 10). This result

implies that the internal region (residues 243 to 463) but not residues 107 to 242 is required for the  $\beta$ -TrCP-dependent degradation of Nrf1. Consistent with this result, internal deletion analysis revealed that  $\beta$ -TrCP siRNA stabilized the M1 mutant (Nrf1 with a deletion of residues 464 through 580) but not the M2 mutant (Nrf1 with a deletion of residues 243 through 580) (Fig. 4A, lanes 11 to 14), emphasizing the functional significance of the region (residues 243 to 463) in the regulation of Nrf1 proteolysis. This result also indicates that the region (residues 107 to 242) is not able to mediate  $\beta$ -TrCP-dependent degradation. Accordingly, we conclude that  $\beta$ -TrCP regulates Nrf1 stability through its internal region (residues 243 to 463).

We also examined the stability of deletion mutants of Nrf1

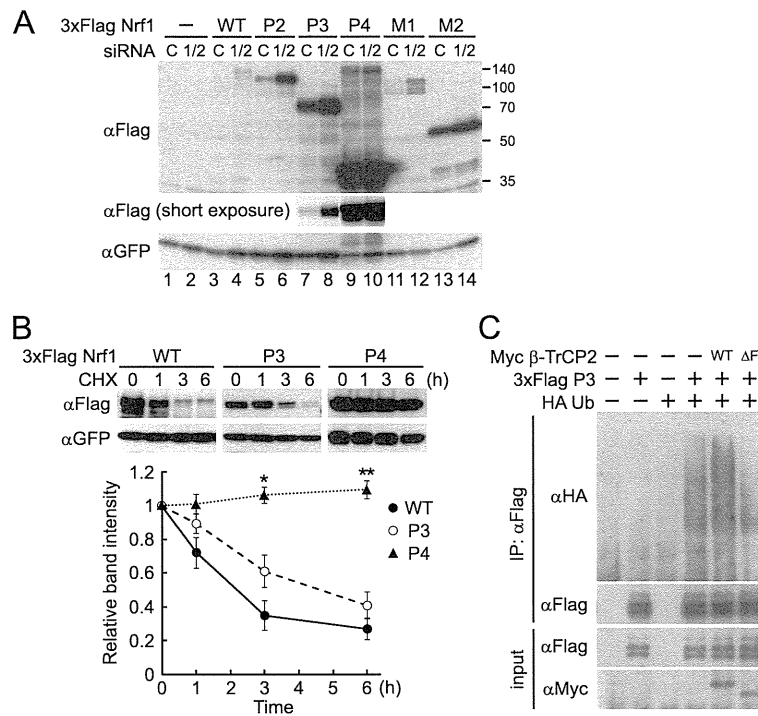


FIG. 4. A region (residues 243 to 463) of Nrf1 is required for its  $\beta$ -TrCP-mediated degradation. (A) The Nrf1 mutants lacking amino acid residues 243 to 463 were not stabilized by the siRNA-mediated knockdown of  $\beta$ -TrCP. Control (C) or  $\beta$ -TrCP (1/2) siRNA was transfected into HeLa cells in combination with the indicated Nrf1 mutants. The expression levels of the mutants were analyzed, as described in the legend to Fig. 2C. (B) The deletion of residues 243 to 463 significantly stabilized Nrf1. HeLa cells were transfected with the expression plasmid for the wild type or the P3 or P4 mutant of 3 $\times$ Flag-Nrf1. Next, the cells were treated with cycloheximide (CHX) (20  $\mu$ g/ml), and the whole-cell extracts were prepared at the indicated time points. The assays were performed three times. Data normalized with cotransfected GFP are presented as the means  $\pm$  standard errors ( $n = 3$ ; \*,  $P < 0.005$ ; \*\*,  $P < 0.001$  versus wild type). (C) The  $\beta$ -TrCP-dependent polyubiquitination of Nrf1 in cultured cells. HeLa cells were transfected with the P3 Nrf1 mutant, HA-ubiquitin (Ub), and the Myc  $\beta$ -TrCP2 wild type (WT) or  $\Delta$ F-box ( $\Delta$ F) mutant. The P3 mutant was immunoprecipitated (IP) by anti-Flag antibody, and its ubiquitination was detected by immunoblot analysis with anti-HA antibody.

by cycloheximide chase experiments to determine whether the internal region identified above is essential for the proteolytic degradation of Nrf1. As a result, the N-terminal-deleted P3 Nrf1 mutant continued to undergo efficient degradation although it was slightly stabilized compared with wild-type Nrf1 (Fig. 4B). In contrast, the P4 mutant, which lacks amino acid residues 243 to 463, was significantly stabilized, indicating that the regulatory motif that is required for the nuclear degradation of Nrf1 resides in this internal region. Overall, we conclude that  $\beta$ -TrCP regulates the nuclear degradation of Nrf1 by associating with its internal region (residues 243 to 463).

**$\beta$ -TrCP mediates the polyubiquitination of Nrf1.** To examine whether  $\beta$ -TrCP mediates the ubiquitination of Nrf1, we performed a ubiquitination assay in cultured cells. The 3 $\times$ Flag-tagged P3 Nrf1 mutant and Myc-tagged  $\beta$ -TrCP2 were cotransfected into HeLa cells along with HA-tagged ubiquitin. The whole-cell extracts were subjected to immunoprecipitation with anti-Flag antibody-conjugated beads, and ubiquitination of the P3 mutant was detected by immunoblotting with anti-HA antibody. This result demonstrates that the ubiquitination of the P3 mutant is markedly enhanced by the coexpression of wild-type  $\beta$ -TrCP2 (Fig. 4C, WT). In addition, the

coexpression of the  $\Delta$ F-box mutant of  $\beta$ -TrCP2 resulted in reduced ubiquitination of the P3 mutant (Fig. 4C,  $\Delta$ F). Thus, we conclude that  $\beta$ -TrCP catalyzes the polyubiquitination of Nrf1 and leads to its proteasome-mediated degradation.

**Identification of the  $\beta$ -TrCP-recognition motif (DSGLS) within Nrf1.**  $\beta$ -TrCP has been characterized as recognizing the consensus motif DpSGX<sub>n</sub>pS ( $n \geq 1$ ; pS represents the phosphorylated serine residue) present in its substrates. We found that certain amino acid sequences (residues 243 to 463) of Nrf1 contain a similar motif, namely, DSGLS (Fig. 5A). Importantly, this motif is highly conserved among species and in other NF-E2-related factors including p45/NF-E2, Nrf2, and Nrf3. Indeed, like Nrf1, Nrf2 was stabilized by knockdown of  $\beta$ -TrCP (Fig. 5B). Prior studies have indicated that the erythropoietin receptor (EpoR) and the YAP transcription coactivator also contain a DSGXS motif that functions as a  $\beta$ -TrCP recognition motif (Fig. 5A) (17, 43). To examine whether this motif is required for the  $\beta$ -TrCP-mediated degradation of Nrf1, we introduced alanine substitutions at two serine residues of the motif Ser448/451, which appear to be the critical phosphorylation sites for  $\beta$ -TrCP binding. We examined the stability of the resultant P3-SA mutant with cycloheximide